2007-11-05

Effect of Beam Splicing on Seismic Response of Buckling-Restrained Braced Frames

Gary S. Prinz
Brigham Young University - Provo

EFFECT OF BEAM SPLICING ON SEISMIC RESPONSE OF BUCKLING RESTRAINED BRACED FRAMES

by

Gary S. Prinz

A thesis submitted to the faculty of

Brigham Young University

in partial fulfillment of the requirements for the degree of

Master of Science

Department of Civil and Environmental Engineering

Brigham Young University

December 2007

BRIGHAM YOUNG UNIVERSITY

GRADUATE COMMITTEE APPROVAL

of a thesis submitted by

Gary S. Prinz

This thesis has been read by each member of the following graduate committee and by majority vote has been found to be satisfactory.

Date	Paul W. Richards, Chair
Date	David W. Jensen Member
Date	Steven E. Benzley Member

BRIGHAM YOUNG UNIVERSITY

As chair of the candidate's graduate committee, I have read the thesis of Gary S. Prinz in its final form and have found that (1) its format, citations, and bibliographical style are consistent and acceptable and fulfill university and department style requirements; (2) its illustrative materials including figures, tables, and charts are in place; and (3) the final manuscript is satisfactory to the graduate committee and is ready for submission to the university library.

Date

Paul W. Richards
Chair, Graduate Committee

Accepted for the Department

E. James Nelson
Graduate Coordinator

Accepted for the College

Alan R. Parkinson
Dean, Ira A. Fulton College of Engineering and Technology

ABSTRACT

EFFECT OF BEAM SPLICING ON SEISMIC RESPONSE

OF BUCKLING RESTRAINED BRACED FRAMES

Gary S. Prinz

Department of Civil and Environmental Engineering

Master of Science

The deformation capacity of typical buckling-restrained braced frames (BRBFs) is limited by the rotation capacity of connecting regions. The rotation capacity of the connection region is limited by fracture of the gusset welds and yielding in the beams and columns. A different connection detail with beam-splices outside the gusset has been shown to increase connection rotation capacity when compared to typical connections, in a few component tests.

This study expands upon the performed component tests, by analyzing the beam splice connection at the system level under directional dynamic loads. Finite element analysis and dynamic loads are used to analyze two 3-story frames having different connection configurations. The first frame has typical BRBF gusset connections, while the second frame has BRBF gusset connections with beam splices. The two frames are dynamically loaded using a recorded earthquake ground acceleration applied at three directions, relative to the frames, and the performance of each frame is compared.

Results indicate that the connections with beam splices effectively prevent large moments from accumulating in the connection regions, reducing gusset stresses. In

addition, the use of beam splices more uniformly distributes the brace load into the beams and columns, and has little effect on in and out-of-plane story drift.

ACKNOWLEDGMENTS

I wish to thank my committee chair, Dr. Paul Richards, for his patience, support, and knowledgeable insights, all of which aided in the quality and timely completion of this document. I also thank Dr. David Jensen and Dr. Steven Benzley for their service as members of my graduate committee. Also, many thanks to Brad Coy whose graduate work aided in the beam-splice design.

I thank my family for their loving support, patience, and guidance throughout my educational time at BYU. In particular I thank my wife Heather, for her kind encouragement and putting up with the many late nights and long days required in completing this document. I also thank my parents, Steve and Debbie, for their examples and encouragement.

TABLE OF CONTENTS

LIST OF TABLES

LIST OF FIGURES

LIST OF TERMS

BRBF	Buckling-restrained braced frame
ULCF	Ultra low-cycle fatigue
SMCS	Stress modified critical strain
RBS	Reduced beam section
A_{BRACE}	Required area of brace core
C_{PR}	Strain hardening factor
Cd	Deflection amplification factor
C_S	Seismic response coefficient
E	Young's modulus of elasticity of steel
F_{BRACE}	Actual resultant brace force
F_U	Ultimate resultant brace force
F_Y	Material yield strength
I_{REQ}	Required moment of inertia
M_F	Maximum allowable moment at moment frame connection
M_{PR}	Plastic moment at location of reduced beam section
R_Y	Material overstrength factor
S_A	Spectral acceleration
S_{DS}	Short-period design response spectral acceleration
S_{D1}	One-second design response spectral acceleration
V_B	Base shear
V_P	Plastic shear at location of reduced beam section
Z_{RBS}	Section modulus of reduced beam section
Z_X	Section modulus
ϕ	Resistance factor

Δ_E	Elastic displacement
Δ_{AE}	Allowable elastic displacement

1 INTRODUCTION

1.1 DESIGN PHILOSOPHY

Design of steel structures for seismic loads generally allows for structural damage during severe seismic events. The typical design objective is to limit material yielding to specific locations and to provide enough ductility in the system to prevent collapse. Such a design is achieved through specially detailed braced frames and moment frames. This thesis discusses one type of ductile braced frame system, called buckling-restrained braced frames (BRBFs).

1.2 BUCKLING-RESTRAINED BRACED FRAMES (BRBFs)

A relatively new type of brace, called a buckling-restrained brace, provides higher ductility than traditional braces. The ductility of traditional braces is limited by poor post-buckling resistance to compressive loads. Buckling-restrained braces have improved ductility, performing equally well in compression and tension (see Figure 1-1) (Tremblay et al., 2006). This symmetric hysteretic behavior is achieved through their composition. Buckling-restrained braces are comprised of a steel core confined in a concrete filled steel casing (see Figure 1-2). The core is designed to axially resist the lateral forces while the concrete confinement prevents local and global buckling of the core. A releasing agent, incorporated between the confining material and core, prevents shear transfer and allows for barreling of the steel when in compression. Since their introduction from Japan to the United States in the late 1990's, buckling-restrained braces have undergone extensive testing by U.S. researchers (Inoue et al 2001; Black et al. 2004; Sabelli et al 2003; Tremblay et al. 2006).

While brace testing demonstrates excellent brace performance (Black et al., 2004), BRBF testing indicates the potential for undesirable failure modes within connected regions (Roeder et al. 2006). These failure modes include: fracture of the beam-to-gusset and column-to-gusset welds, beam local buckling, and column local buckling (see Figure 1-3).

A prototype BRBF connection tested by Coy (2007) prevented damage to the gusset, beam, and column through the use of beam splices. The connection used flange connector plates across the splice (see Figure 1-5) and was modeled after a similar design proposed by Walters et al. (2004) which had both web and flange connector plates. With the connector plates only located at the top flange, the entire lateral load is transferred at the flange level, precluding a moment couple between the splice connection and concrete slab. Component testing of the beam-splice BRBF connection sustained drifts in excess of 6 percent with inelastic deformation limited to the flange connector plates. The loading was applied in the plane of the BRBF.

A full-scale four story frame tested by Fahnestock et al. (2007) incorporated BRBFs with beam splice connections. The splice connections were located outside the gussets with T-beams joining the beam sections at the web (see Figure 1-4). Testing results from pseudo-dynamic loading show the connection sustained frame drifts of near 0.05 rad, exceeding typical BRBF frame drift capacity which is between 0.02 and 0.025 rad (Fahnestock et al. 2007). The frame was subjected to in-plane loading only.

1.3 FINITE ELEMENT ANALYSIS

Finite element analysis is a useful tool for analyzing structures with complex loads. Most of the research with finite element analysis has used statically applied loads where the materials are free from inertial influence. Due to the required computational demands, there has been minimal investigation of building structures using dynamic loads. The dynamic load research that has been conducted mainly involves explicit analysis of blast loadings on structural components and vibration modes of mechanical structures (Koh et al. 2003; Shahkarami and Vaziri 2007).

Richards and Prinz (2007) investigated the benefits of using models with shell elements in connection regions over traditional models with beam elements, for dynamic analysis. The models with beam elements required predetermined regions of lumped plasticity, whereas the models with shell elements only required material properties and model geometries to determine the occurrence of material non-linearity. In addition, the models with shell elements have the capability to predict the onset of low-cycle fatigue, a common limit state in ductile steel systems.

1.4 PREDICTING LOW-CYCLE FATIGUE

Over the past 30 years, efforts to predict the onset of ultra low-cycle fatigue (ULCF) resulted in a failure index, relating strain capacities and demands (Fell et al., 2006). The failure index is determined by dividing equivalent plastic strain with a critical plastic strain obtained using a stress modified critical strain (SMCS) criterion (Chi et al., 2004). To validate the failure index, Fell et al. (2006) compared a finite element model of a special concentrically braced frame with a full scale specimen having an identical geometry. The failure index predicted an identical crack initiation location as observed in the full-scale test.

1.5 OBJECTIVE

The aim of this study is to expand upon the research performed by Coy (2007) by analyzing the beam-splice flange connection at the system level under directional dynamic loads. A dynamic study lends itself to shake-table testing with full-scale steel specimens; however, shake-table testing is expensive and requires extensive laboratory resources. In addition, full-scale testing is time intensive, requiring fabrication and construction of test specimens. Validated computer models are a less expensive and time saving method for obtaining data from 3-dimensional dynamic loading.

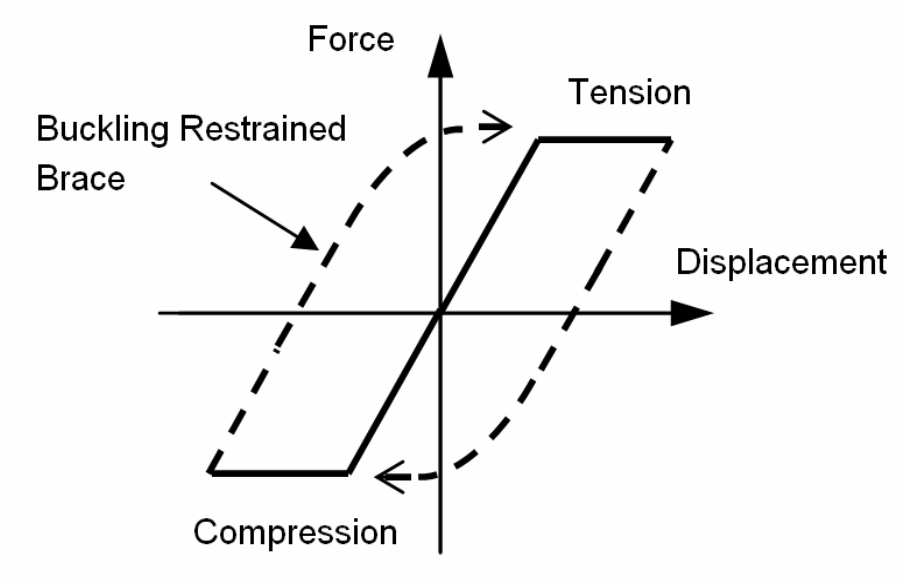

Figure 1-1 BRBF hysteretic behavior

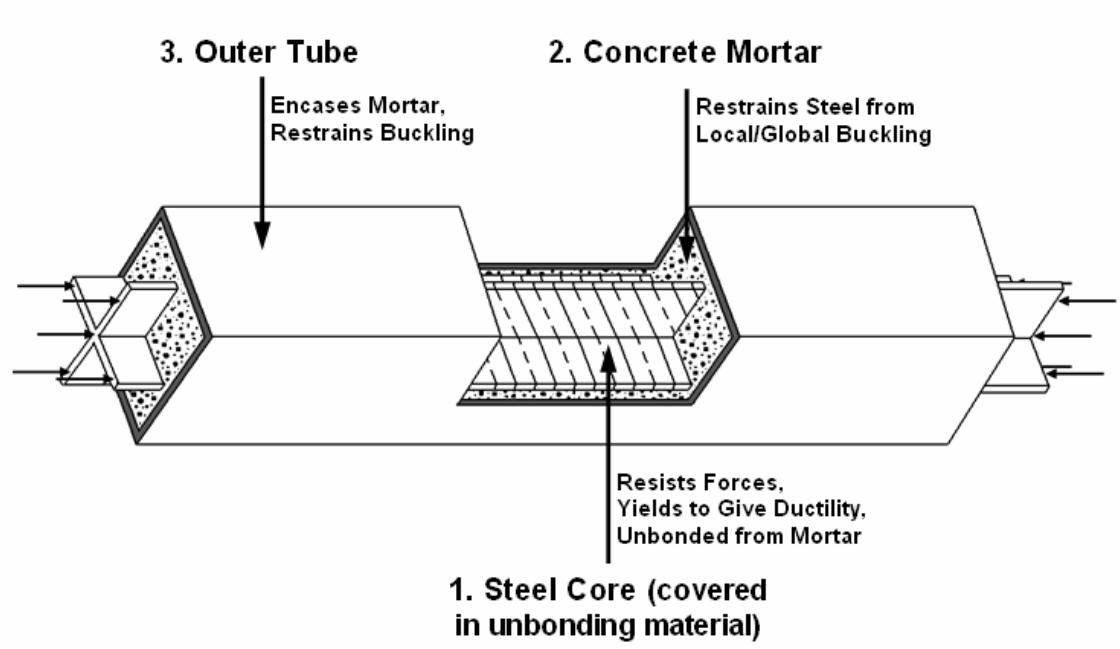

Figure 1-2 Buckling-restrained brace schematic (Coy, 2007)

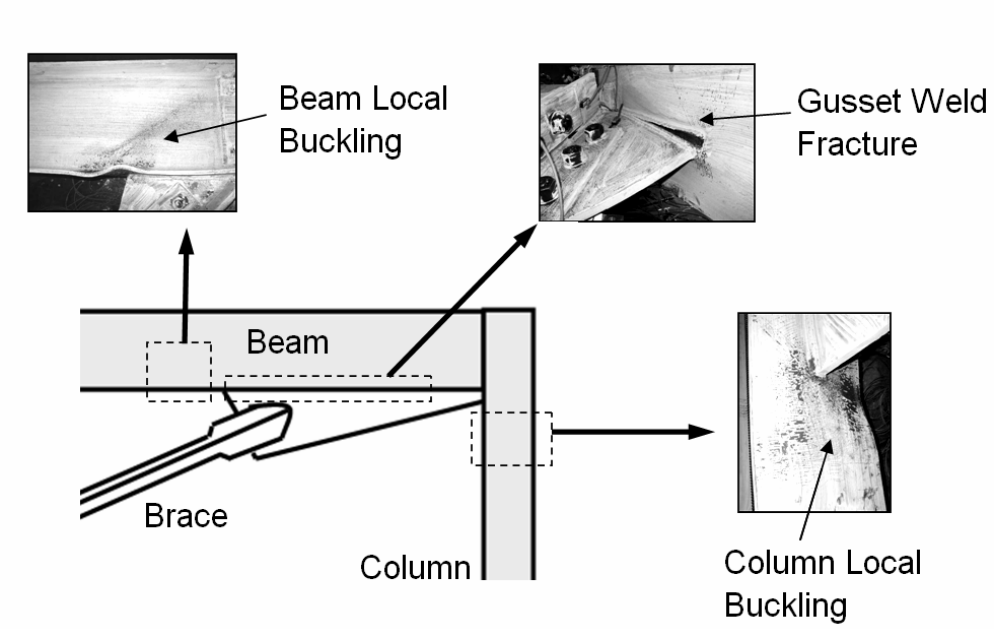

Figure 1-3 BRBF connection failures

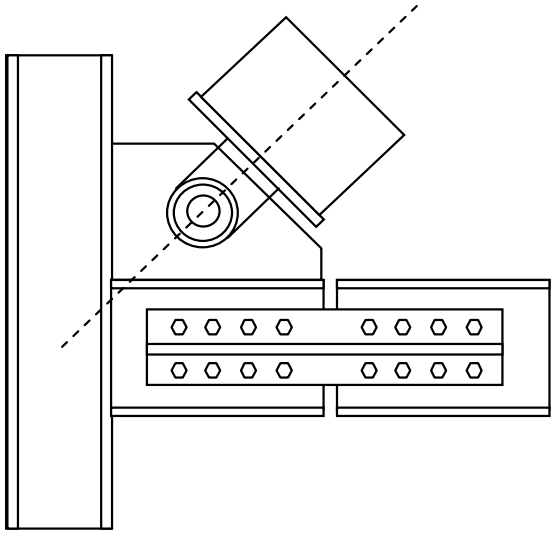

Figure 1-4 Lehigh pinned connection with web splice (Coy et al., 2007)

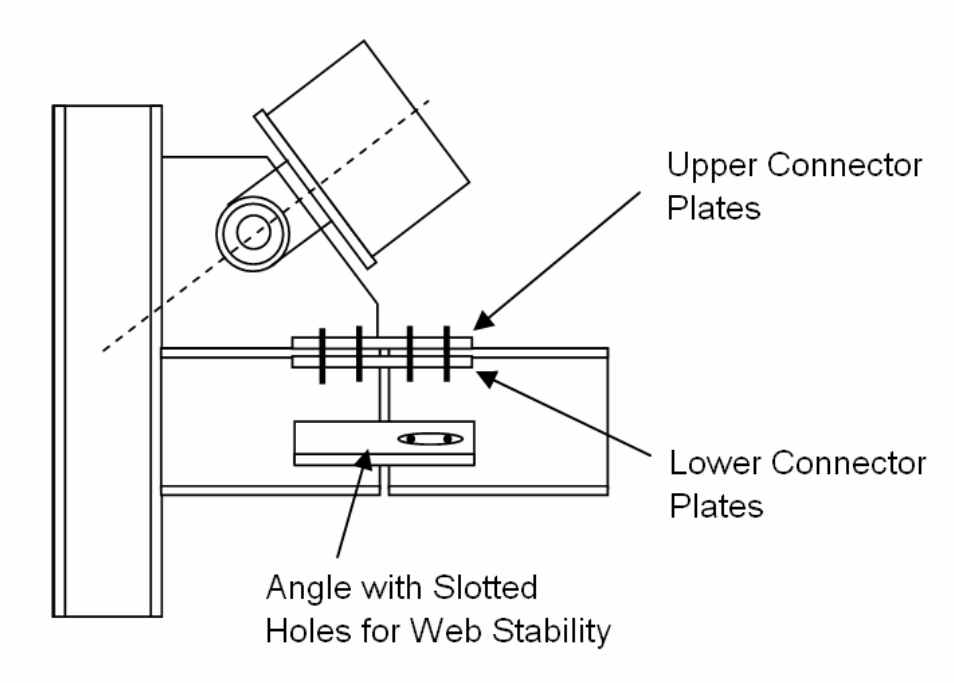

Figure 1-5 Pinned connection with flange connector plates (Coy et al., 2007)

2 COMPUTER SIMULATIONS

In this study, finite element analysis was used to compare the behavior of two 3-story BRBFs having different gusset connections. The two frames were dynamically loaded at three different angles resulting in a total of six analyses. Shell elements were used in modeling the connection regions. The first frame had typical BRBFs gusset connections. The second frame incorporated a prototype BRBF hinged gusset connection with beam splices. Figure 2-1 shows a side-by-side comparison of the typical BRBF connection and the hinged BRBF connection. All analyses were performed using the commercial finite element program ABAQUS (HKS, 2006).

Validation of modeling techniques and fracture prediction methodologies was performed prior to the development of the 3-story frames. Validation studies are presented at the end of this document in Appendices A through D. Material properties, boundary constraints, mesh refinement, and fracture prediction methodologies validated in these studies were utilized in the 3-story test models.

2.1 DESIGN OF PROTOTYPE BUILDING

2.1.1 General

A three story building was designed with BRBFs in one direction and special moment frames in the other. A plan view of the designed building is shown in Figure 2-2. Exploiting symmetry, only one quarter of the building's seismic system was designed. The bay dimensions (see Figure 2-2) and floor masses used in the design were taken from a SAC study (Gupta and Krawinkler, 1999). The seismic weight for the entire three story building is 6,503 kips and the location and configuration of the BRBFs and special moment frames are shown in Figure 2-2. A Los Angeles, California site was used

for design with S_{DS}=1.12 and S_{D1}=0.60, where S_{DS} and S_{D1} are the site design spectral accelerations at 0.2 and 1.0 seconds in terms of gravity. Figure 2-3 shows the design response spectra.

Figure 2-4 shows the member sizes selected for the BRBF and special moment frame bays, as well as the designed brace cross-sectional area. The BRBF beams attach to the weak axis of the moment frame column (see Figure 2-4).

2.1.2 Special Moment Frame Design

The special moment frame design followed the equivalent lateral force method outlined in ASCE-07 (ASCE, 2005). Member sizes for the special moment frame bays were governed by drift requirements. Reduced beam sections (RBSs), common in post Northridge moment frames, were used in the special moment frame design (see Figure 2-5). For detailed special moment frame and RBS design calculations see Appendix B.

2.1.3 BRBF Design

The BRBF columns and beams were designed to resist ultimate brace forces. The buckling-restrained braces of each bay primarily resist axial loads; therefore, design of each brace involved a required cross-sectional area to resist the brace force. For detailed BRBF design calculations see Appendix B.

Coy (2007) outlined design guidelines for the BRBF hinged connection (Figure 2-6). Following the guidelines, a 1 ¼" gap, located 2" from the gusset connection, was introduced to the BRBF beam. The beam gap was then spliced using bolted rectangular steel plates connected at the top flange (see Figure 2-6). The location of the splice connection results in the transfer of load through the beam top flange. The brace angle is selected to facilitate the working point at the intersection of the beam top flange and column web center (see Figure 2-7). Because the seismic loads increase with building height, design of the connector plates and number of bolts vary at each story-level. Table 1 gives the specified connector plates and number of bolts for each story level.

2.2 MODELING TECHNIQUES

2.2.1 General

The computer models represent the lateral force resisting system for one quarter of a building (see Figure 2-8 and Figure 2-2). The remaining structure (concrete slab and gravity bays) were modeled using boundary conditions.

To simulate the action of a concrete slab, column displacements within each floor level were constrained to be equal. This is justified based on the assumption that the slab acts as a rigid diaphragm. The equal column displacements were accomplished by implementing rigid-body nodal constraints at the center of each column (floor-level). The bases of the columns were fixed simulating a rigid foundation. Figure 2-9 shows the imposed constraints on the model.

Mesh size and element type affect the accuracy of analysis. The computer models analyzed in this study utilized four-node linear quadrilateral elements at a general mesh size of 2" in the connection regions. In regions of interest, regions with the highest potential for ultra-low cycle fatigue, the mesh size was reduced to 1" for improved strain accuracy. The mesh refinement was implemented at the RBS of the moment frames and in the splice connector plates of the BRBF hinged connection. Figure 2-10 shows the refined mesh at the RBS and BRBF splice plates.

In regions with simple geometry and no expectation of yielding, 1-dimensional Timoshenko beam elements were inserted to replace the shell elements and reduce computational expense. At the interface between the shell and beam elements, rigid-body nodal ties of each type of element were referenced to a common node. Figure 2-11 shows a representation of this element transitioning process.

All material properties were obtained from cyclic coupon testing and 5 percent stiffness proportional damping was specified in the first mode.

2.2.2 BRBF Specific

To simulate confinement of the brace core and prevent the brace from buckling out of plane, rotation constraints (both in and out of plane) were implemented along the brace length (see Figure 2-9). Based on a drift of 4%, the brace core was calculated to

strain 3” out of the confining material; therefore, the rotation constraints were not implemented within 3” of the brace connection.

In modeling the hinged BRBF connection, the connector plates were spaced away from the beam flange using bolts. The spacing corresponded to the plate centerline location (see Figure 2-12). This modeling technique is validated in Appendix C. The connecting bolts were modeled using 1-dimensional Timoshenko beam elements with 7/8” diameter bolt area properties. Bolt slipping was not introduced into the models.

Figure 2-13 shows the multi-linear stress-strain curve used for the brace material property. The stress-strain relationship was determined from material testing (Coy, 2007). The resulting slope at each strain interval is determined from the material elastic modulus and yield stress. For the purpose of this study, the brace material yield stress is considered to be 46 ksi.

2.2.3 Frame Loading

The test models were loaded using a scaled version of an acceleration record obtained from the Loma Prieta, California earthquake. The scaling is done to match the design response spectra at the period of the frame being modeled. The scale factor used is 3.53. A superimposed plot of the scaled spectra and design spectra is shown in Figure 2-14.

Three different directions of the ground acceleration, relative to the model, were considered in this study. The relative directions include: 0° (plane of the BRBF), 45°, and 90° (plane of the special moment frame).

2.3 FATIGUE FAILURE INDEX

Ultra-low cycle fatigue (ULCF) fracture is the ductile fracture mechanism of materials subject to large plastic strains. ULCF is a governing mode of failure in ductile steel systems.

The method used in this study to predict low-cycle ductile fracture involves a combination of stress and strain states incorporated into a failure index. The failure index is determined by dividing equivalent plastic strain (PEEQ) with a critical plastic strain

obtained using a stress modified critical strain (SMCS) criterion. Equivalent plastic strain is defined using the plastic strain rate tensor $\dot{\varepsilon}_{ij}^{P}$ in the equation:

$$\text{PEEQ} = \int_0^t \sqrt{\frac{2}{3}\dot{\varepsilon}_{ij}^{P}\dot{\varepsilon}_{ij}^{P}}\, dt \tag{2. 1}$$

The critical plastic strain is taken as:

$$\varepsilon_{p_{CRITICAL}} = \alpha \cdot \exp\left[-1.5 \cdot \frac{\sigma_m}{\sigma_e}\right] \tag{2. 2}$$

(Hancock and Mackenzie, 1976) where σ_m is the mean stress, σ_e is the von Mises stress, and α is a material constant obtained from coupon testing. For the purpose of this study, α is considered to be 2.6 (Chi et al. 2004). When the equivalent plastic strain exceeds the critical value $\varepsilon_{P\ CRITICAL}$, fracture initiation begins; thus, a failure index greater than 1 indicates fracture initiation.

Table 2-1: Bolt and Connector Plate Specifications.

		Upper Connection [1]	
		Top Plate[2]	Bottom Plates[2]
Floor 1	Plates	27.125 x 6.5 x 1.125	27.125 x 3.25 x 1.125
	7/8" bolts/plate	8	8
Floor 2	Plates	21.125 x 6.5 x 1	21.125 x 3.25 x 1
	7/8" bolts/plate	6	6
Roof	Plates	15.125 x 3 x 3/4	15.125 x 3.25 x 5/8
	7/8" bolts/plate	4	4
		Lower Connection[1]	
		Top Plates[2]	Bottom Plates[2]
Floor 1	Plates	27.125 x 3.125 x 1.125	27.125 x 3.25 x 1.125
	7/8" bolts/plate	8	8
Floor 2	Plates	21.125 x 3 x 1	21.125 x 3.25 x 1
	7/8" bolts/plate	6	6
Roof	Plates	NA	NA
	7/8" bolts/plate	NA	NA

[1] Terminology described in Figure 2-7
[2] Terminology described in Figure 2-6

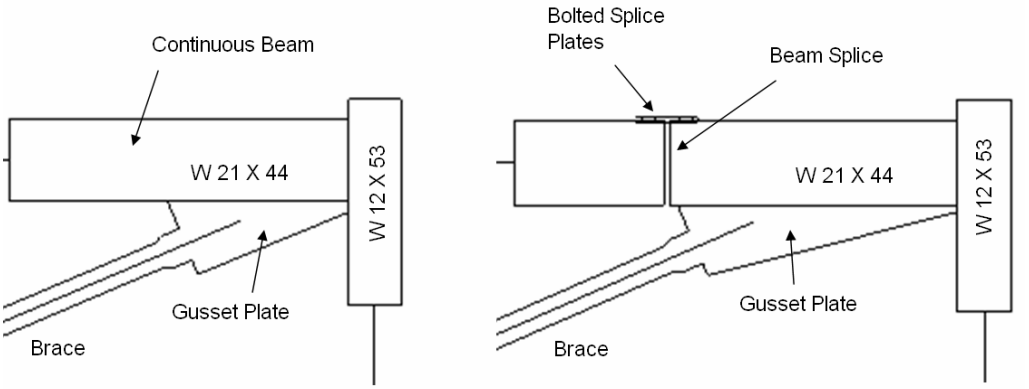

(a.) **(b.)**

Figure 2-1 (a.) Typical BRBF connection; (b.) hinged BRBF connection

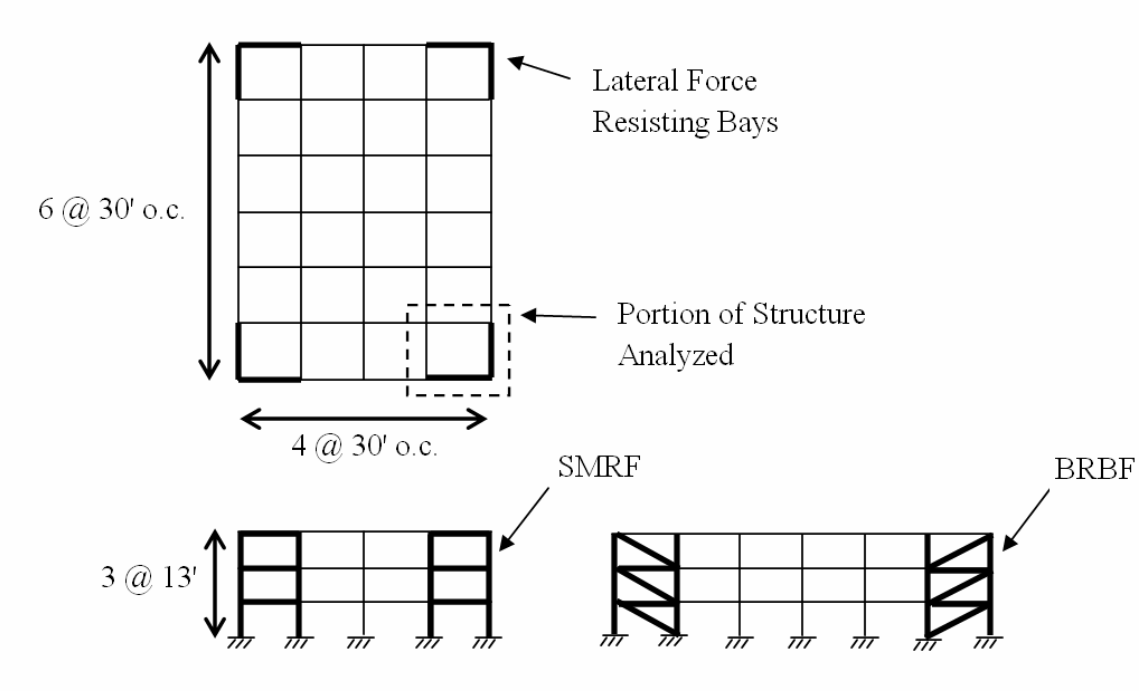

Figure 2-2 Plan and elevation view of 3-story building

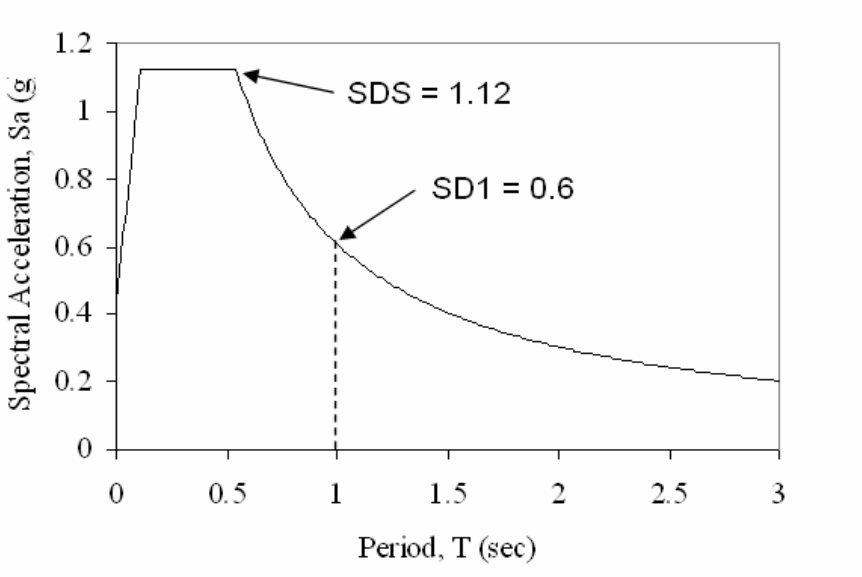

Figure 2-3 Design response spectra

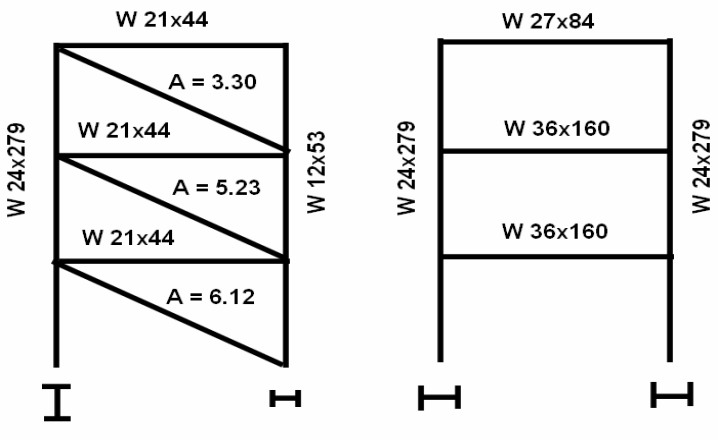

Figure 2-4 BRBF and special moment frame member sizes

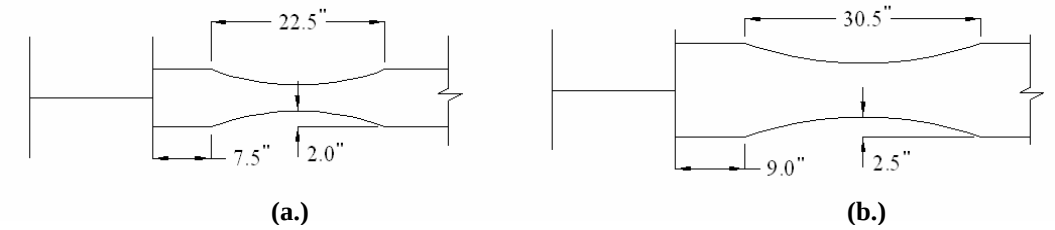

(a.) **(b.)**

Figure 2-5 (a.) RBS roof; (b.) RBS floors 1&2

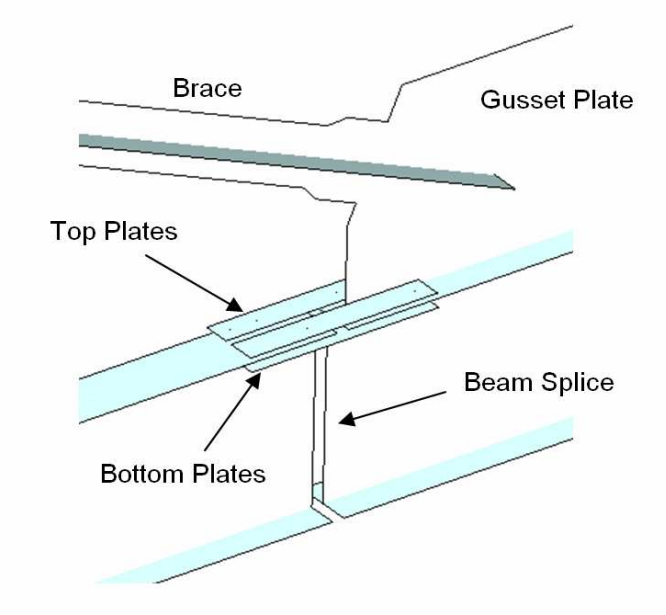

Figure 2-6 Representation of rectangular splice plates

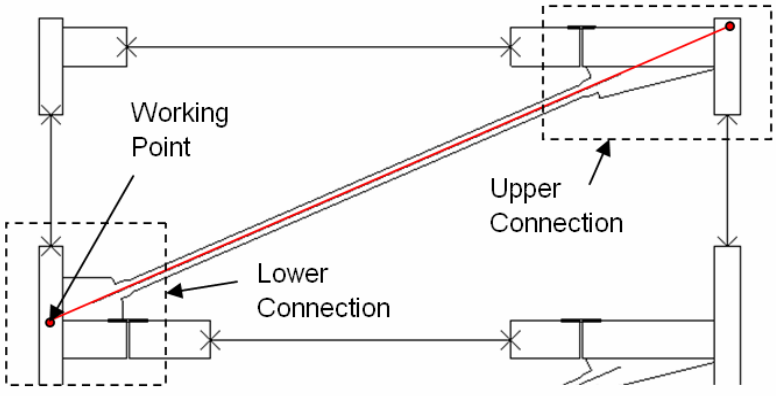

Figure 2-7 BRBF hinged beam working point

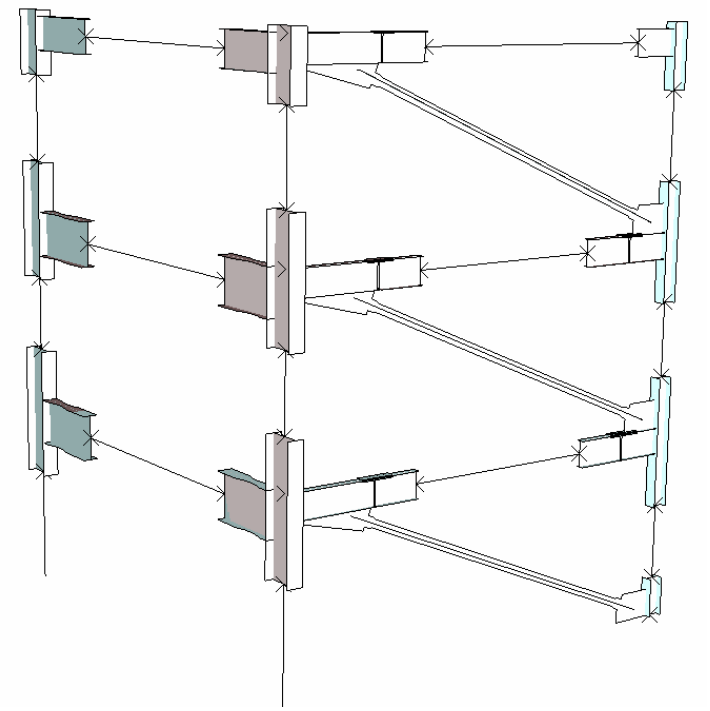

Figure 2-8 Computer model of test frames

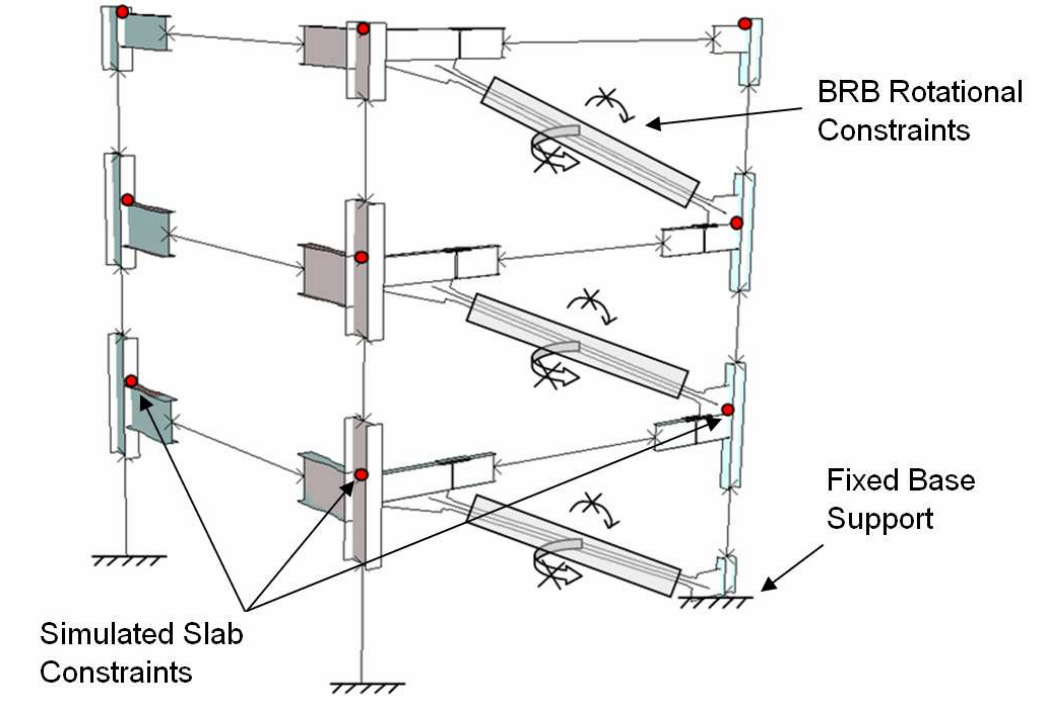

Figure 2-9 Test model with boundary constraints

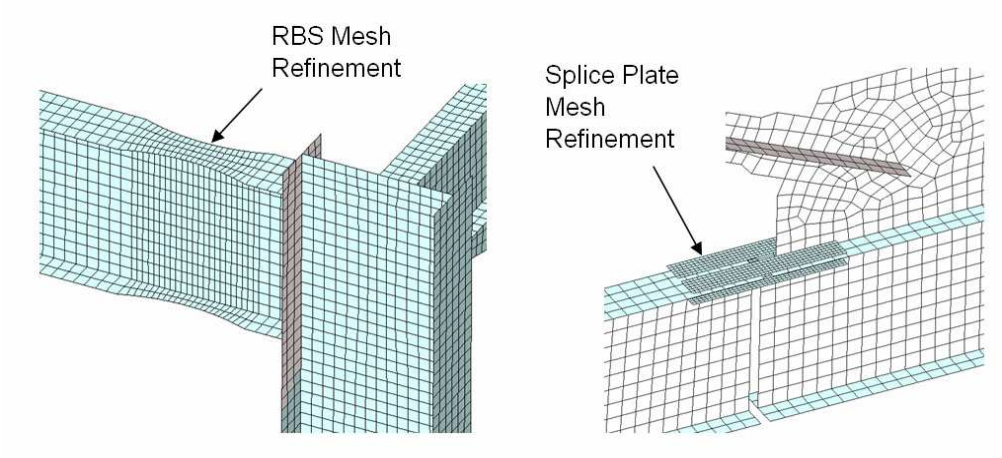

Figure 2-10 Mesh refinement at RBS and splice plate regions

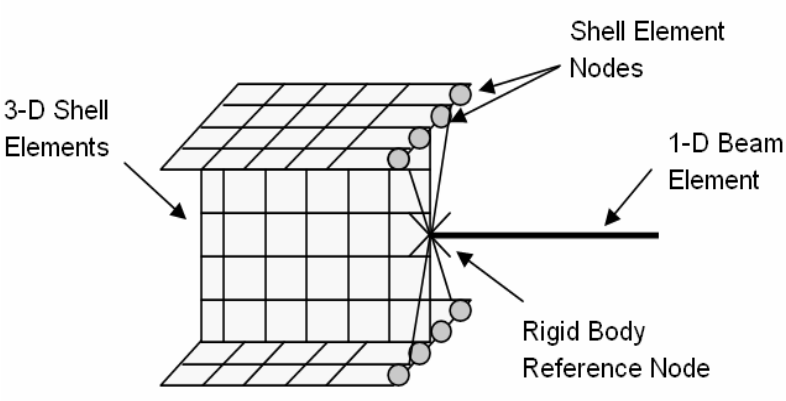

Figure 2-11 Beam to shell element transition

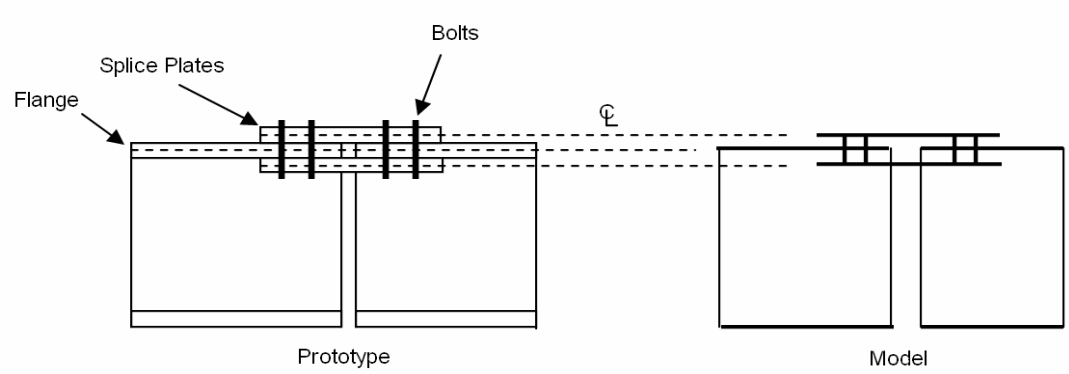

Figure 2-12 Representation of connector-plate gap with shell elements

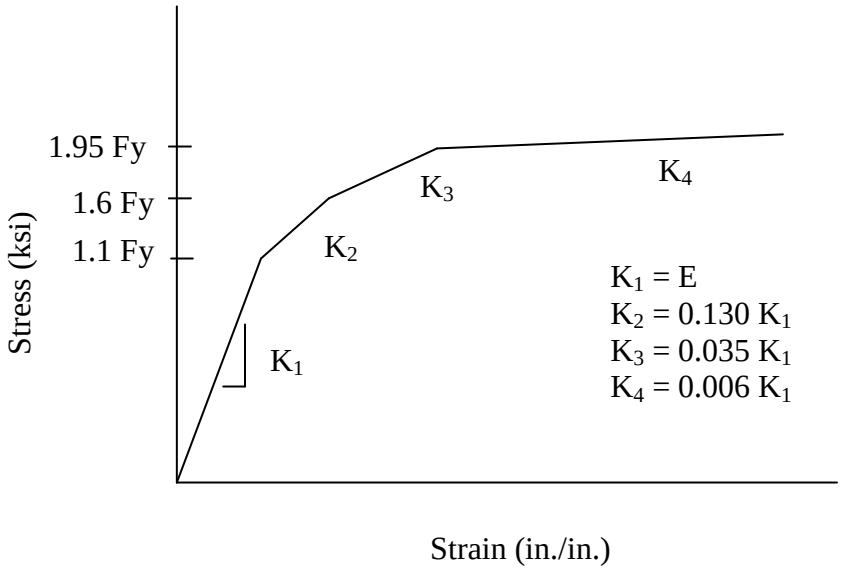

Figure 2-13 Brace general material stress strain curve

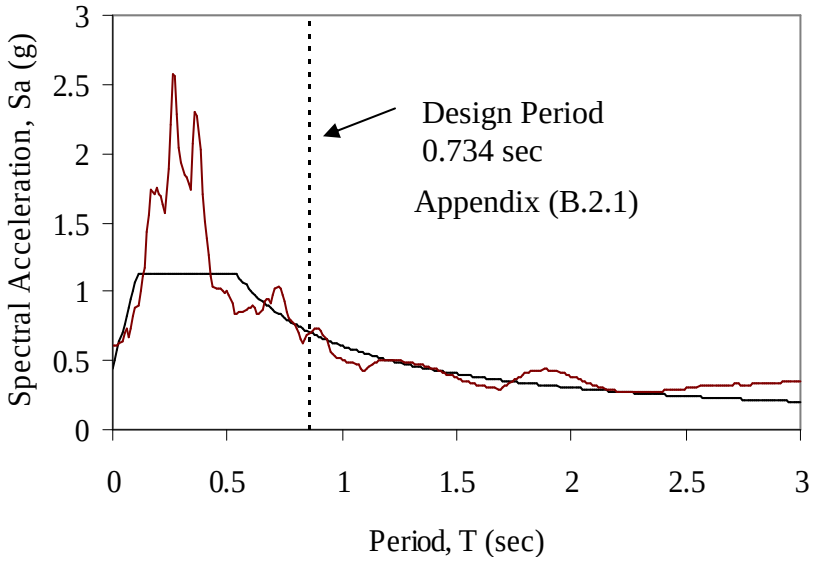

Figure 2-14 Design spectra and scaled response spectra

3 RESULTS AND DISCUSSION

Story drifts, gusset plate connection stresses, and failure index values from the analyses are presented in the following sections.

3.1 STORY DRIFT

In-plane story drifts for both test frames are presented in Figure 3-1. Drift is maximum relative floor displacement divided by story height. Story drifts for the hinged case are within 3 percent of those for the unhinged case. Story drifts for the two frames differed by less than 5 percent when loaded in the out-of-plane directions. The similarities in drift indicate that splicing the beam and creating a hinge connection has minimal effect on story drift.

In-plane story drift values of the BRBFs decreased as the loading direction changed from 0 to 45 degrees. The maximum BRBF drifts for the 45 degree out-of-plane loading were nearly 30 percent less than those recorded from the BRBF in-plane loading. This is expected, since only 70.7 (cos 45°) percent of the load is acting in-plane.

3.1.1 Observations

Under all three loading directions, yielding of the BRBFs was limited to the brace cores. Each brace core had an area of uniform yielding within the region of simulated confinement (see Figure 3-3). Torsion in the BRBF beams was observed during out-of-plane loading (see Figure 3-2). The beam torsion did not cause plastic strains in the splice plates.

3.2 GUSSET-PLATE CONNECTION STRESS

To compare the different frame connections, stresses were taken at the analysis time corresponding to maximum BRBF drift. This comparison of gusset stresses is valid due to the similar maximum drift values between the two models (see Figure 3-1). The distribution of stress in each beam-to-gusset and column-to-gusset connection is presented in Figure 3-4 through Figure 3-13.

Splice plate deformation in the hinged specimen allowed the beam at the gusset connection and column to remain perpendicular as the frame deformed laterally, resulting in reduced moments at the beam-column interface. In the typical frame connection, there was no hinge mechanism to prevent moments from developing, resulting in higher stresses at the ends of the gusset connections.

3.2.1 BRBF In-Plane Loading

The distribution of von Mises stress along the beam in the 1st floor upper gusset connection is shown in Figure 3-4. The stress values indicate the hinged connection evenly distributes the stresses along the gusset-to-beam connection (a slight peak in the middle) while the unhinged specimen stress values increase away from the column. The stress increase in the unhinged connection is somewhat linear. The maximum gusset stress in the unhinged connection is 63.56 ksi which is over 2 times larger than the highest stress in the hinged connection (29.69 ksi).

The distribution of stress along the beam is shown in Figure 3-5 and the stress along the column in the 1st floor lower gusset connection is shown in Figure 3-6. Stress from the two plots show that the beam-to-gusset connection transfers most of the brace load (nearly twice that of the column connection). Again, maximum stresses for the unhinged connection are nearly 2 times larger than the hinged connection.

3.2.2 BRBF Out-of-Plane Loading

The stress values recorded from the 45 degree loading exhibit similar patterns found with the in-plane loading (see Figure 3-7 and Figure 3-13). With the exception of the 1st floor upper hinge connection, the 45 degree stress values are less in magnitude (20

to 50 percent less) than the in-plane stress values. At the end of the gusset plate, stresses in the upper connection on the 1st floor exceeded those recorded from the in-plane loading (see Figure 3-7). The increase can be explained by beam torsion. Stress values for the 90 degree loading were negligible (maximum value less than 1 ksi) and therefore are not represented in the figures.

3.3 FATIGUE FAILURE INDEX PREDICTION

The yielding portion in the 2nd floor brace core (see Figure 3-3) had the greatest accumulation of plastic strain. At this critical location, element stress and strain data were used to compute the failure index. The failure index for this location reached a maximum value of 0.0127. This value is much less than the critical failure index value of 1 (see Figure 3-14), indicating that the brace core material would not experience low-cycle fatigue cracks. If this were an actual steel structure, only minor structural repairs would be necessary.

The failure index value for the different story-level brace cores at each loading angle is shown in Figure 3-15. As the load moves away from the plane of the BRBFs, the failure index value decreases. This corresponds with a reduction in brace core yielding. The failure index for the 90 degree loading is 0 because the brace cores did not yield. The failure index values for the hinged connection are larger than those for the unhinged connection (see Figure 3-15).

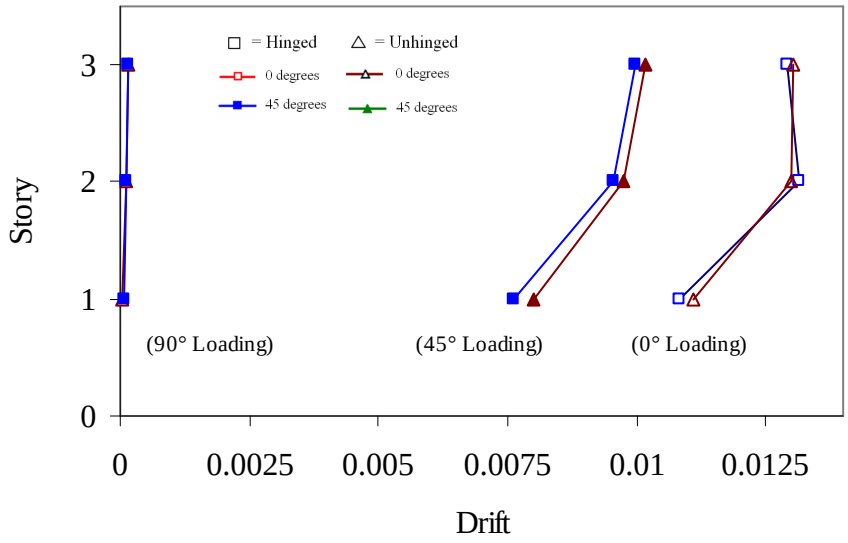

Figure 3-1 BRBF drift under 0, 45, and 90 degree excitations

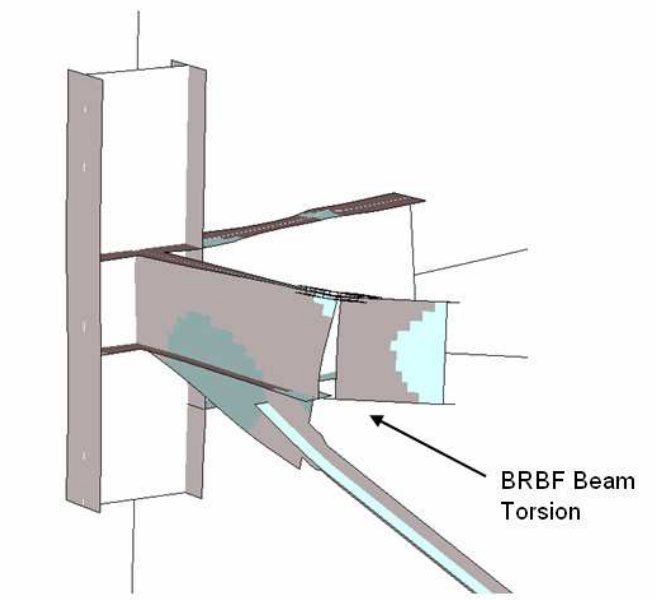

Figure 3-2 Beam torsion during 45 degree out-of-plane load (scaled 10x)

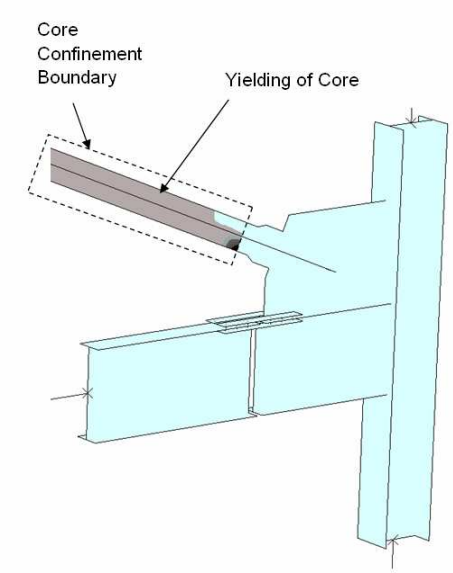

Figure 3-3 Yielding in hinged BRBF connection region

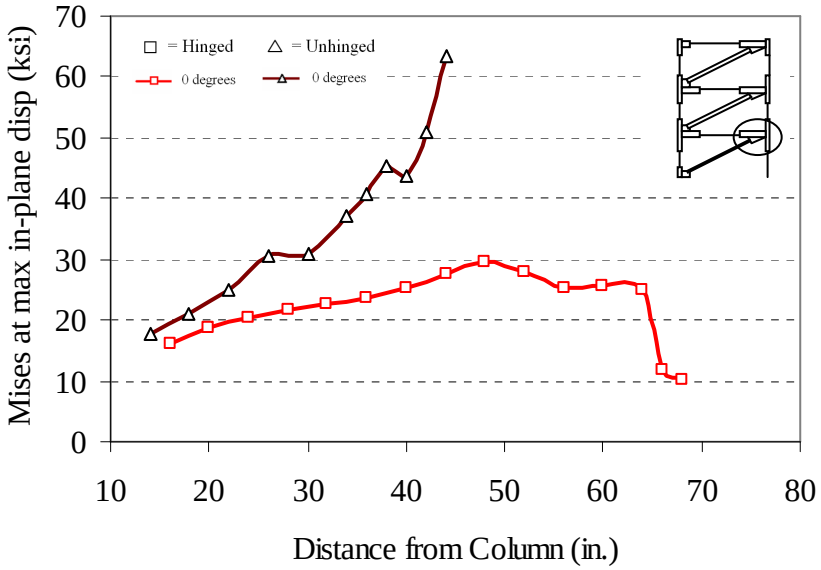

Figure 3-4 1st floor upper beam-to-gusset connection stresses (In-plane loading)

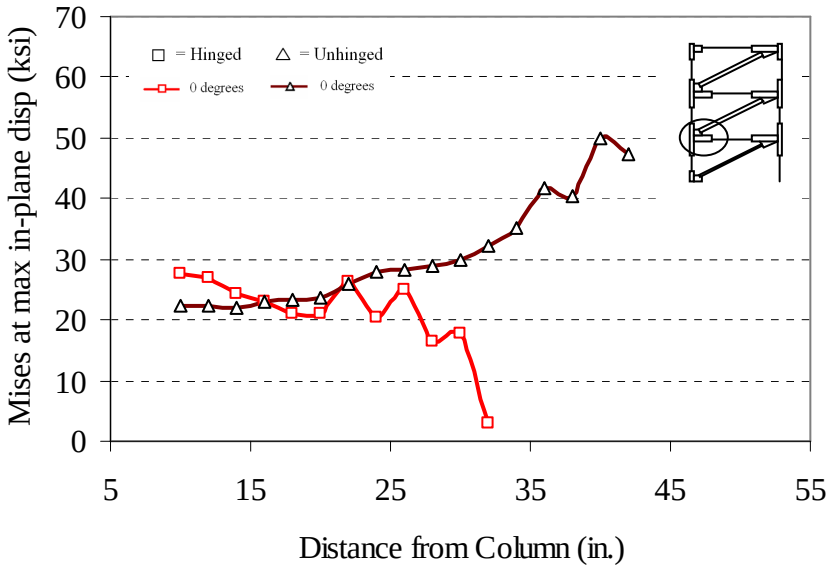

Figure 3-5 1st floor lower beam-to-gusset connection stresses (In-plane loading)

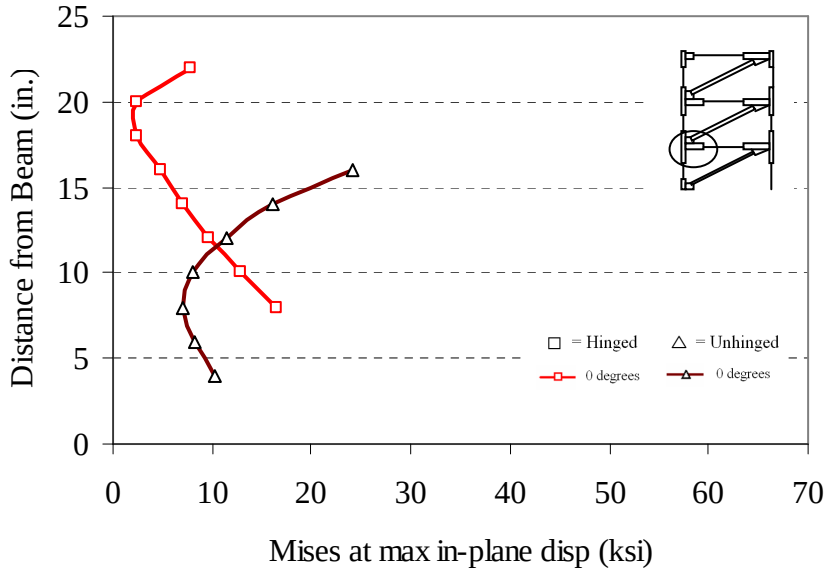

Figure 3-6 1st floor lower column-to-gusset connection stresses (In-plane loading)

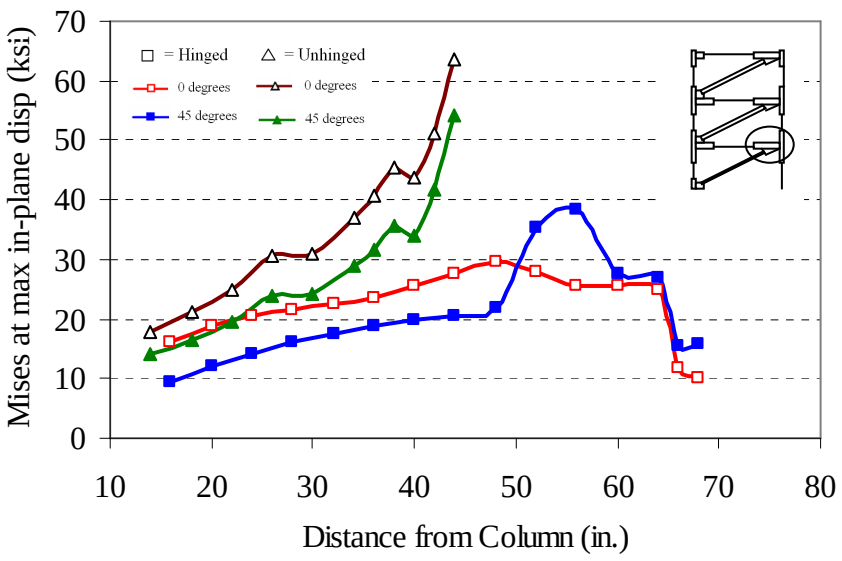

Figure 3-7 In and out-of-plane upper beam-to-gusset connection stresses (0 and 45 degrees)

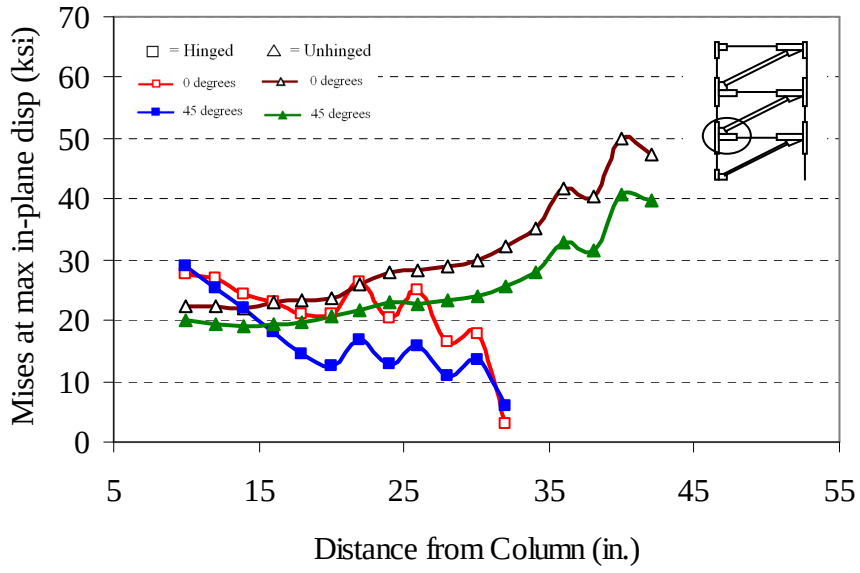

Figure 3-8 In and out-of-plane lower beam-to-gusset connection stresses (0 and 45 degrees)

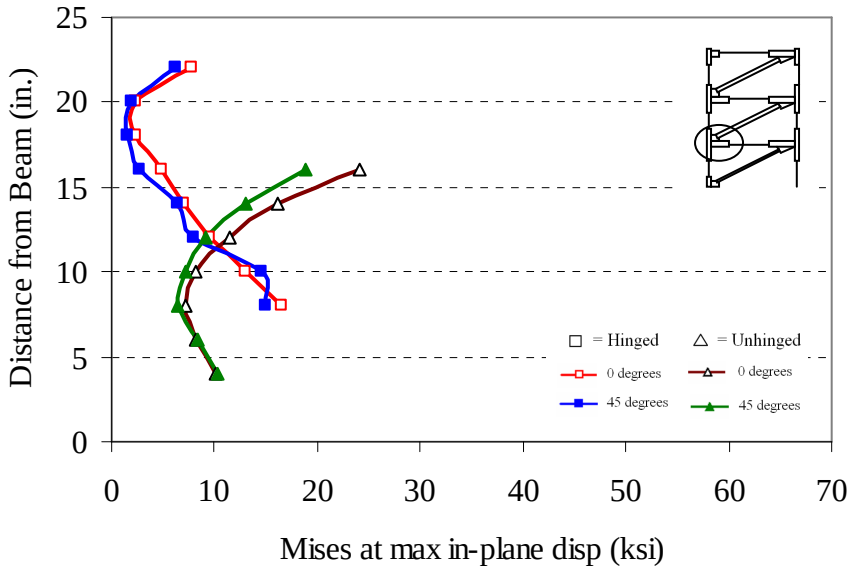

Figure 3-9 In and out-of-plane lower column-to-gusset connection stresses (0 and 45 degrees)

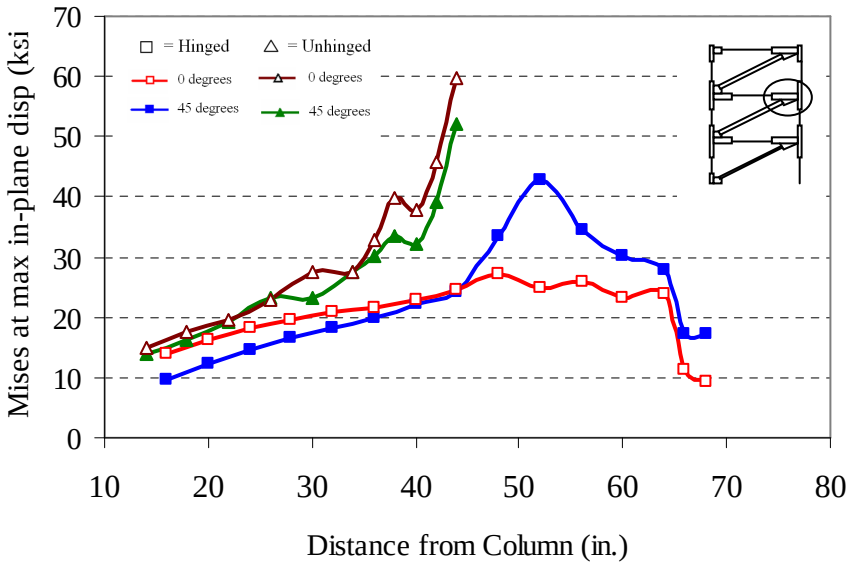

Figure 3-10 Stress distribution for floor 2 upper gusset-to-beam connection

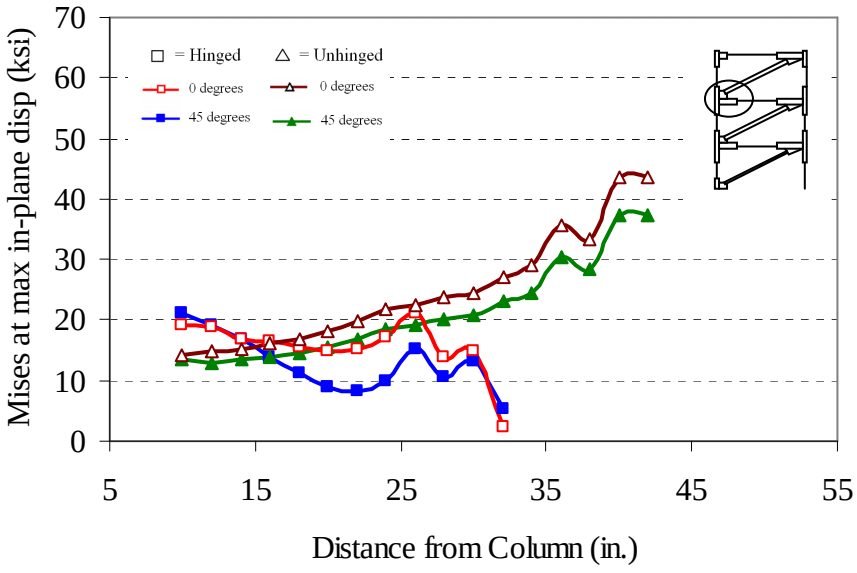

Figure 3-11 Stress distribution for floor 2 lower gusset-to-beam connection

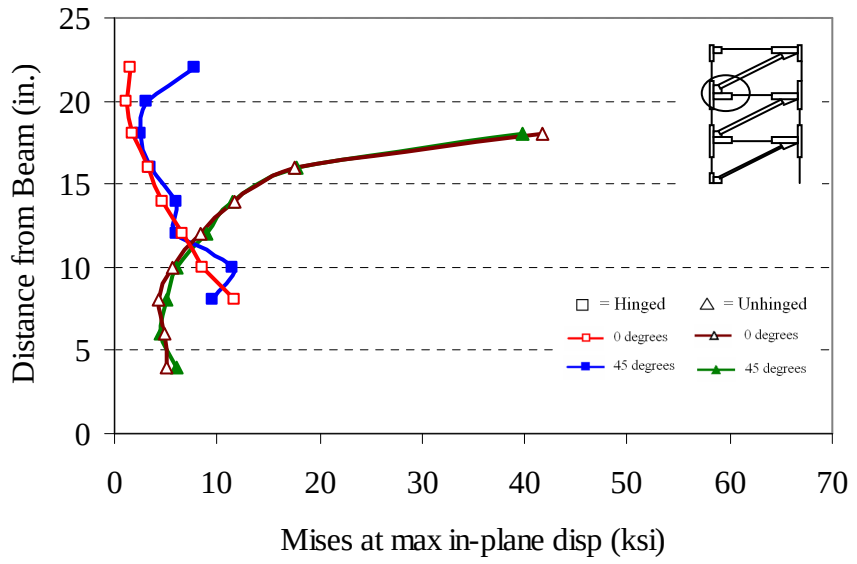

Figure 3-12 Stress distribution for floor 2 lower gusset-to-column connection

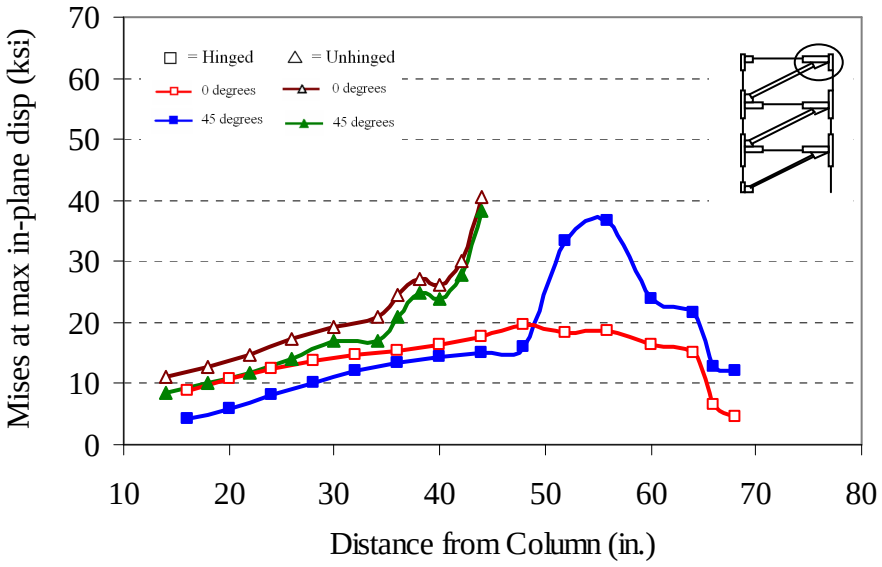

Figure 3-13 Stress distribution for floor 3 upper gusset-to-beam connection

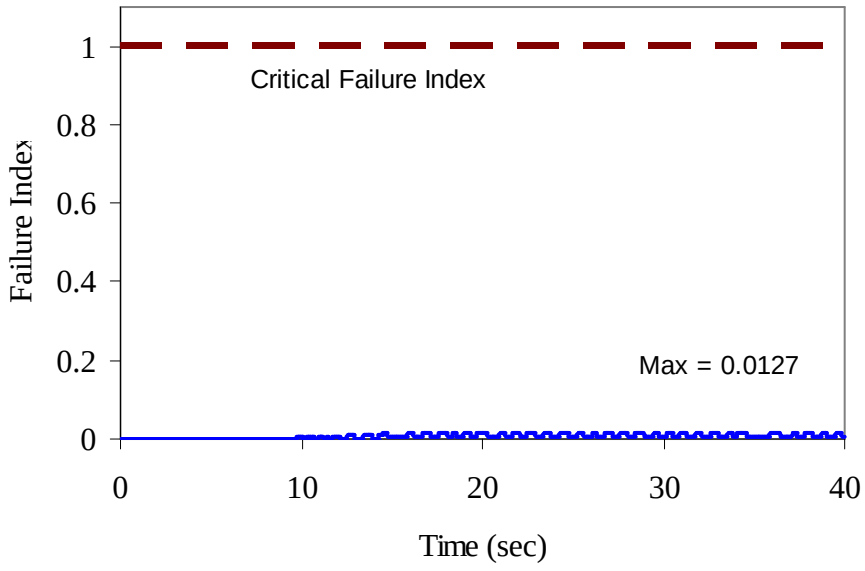

Figure 3-14 Failure index in level 2 brace core

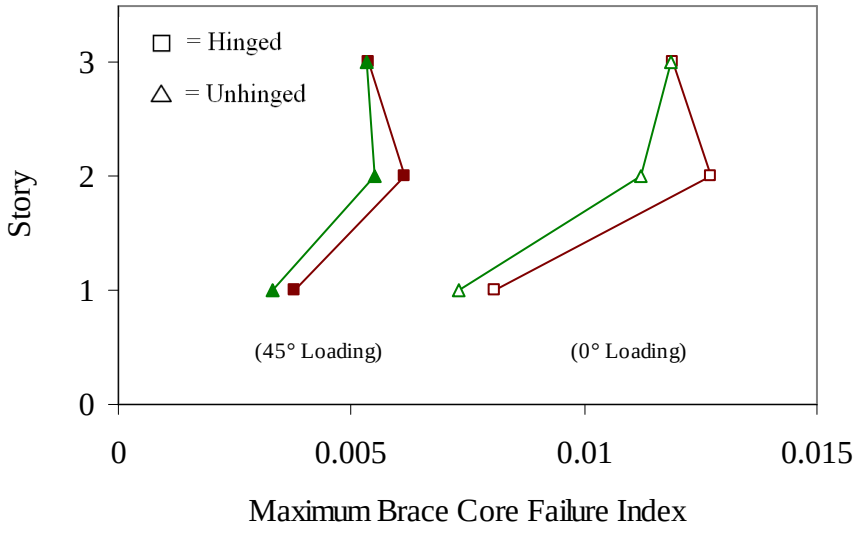

Figure 3-15 Maximum brace core failure index values

4 CONCLUSIONS AND RECOMMENDATIONS

In this study, finite element analysis with dynamic loading was used to assess BRBF out-of-plane behavior and the effects of beam splices in improving BRBF connection rotation capacity. Earthquake ground accelerations applied at three different angles provided dynamic building loads comparable to design-level seismic events.

4.1 SPLICE PLATE SYSTEM-LEVEL PERFORMANCE

The frame with hinged connections was effective in reducing moments and stress concentrations in the gusset-to-beam and gusset-to-column connecting regions, compared to the unhinged connection. Maximum gusset stresses in the first story beams and columns had a 50 percent reduction in magnitude without any stiffness or strength degradation. The hinging action of the splice plates prevented large moments in the connection regions and more uniformly distributed the brace load into the beams and columns. Without such a ductile mechanism, the typical connection experienced stress concentrations at the ends of the gusset plates. The reduction in gusset connection stresses due to the hinged region indicates that beam splicing can aid in preventing non-ductile failure modes (fracture in the gusset-to-beam and gusset-to-column welds) which plague typical BRBF connections.

4.2 OUT-OF-PLANE BRBF BEHAVIOR

Both the hinged and typical test frame connections performed well under out-of-plane loading. The out-of-plane loads had little effect on splice plate or brace performance. Connection stresses and story drifts were reduced as components of the

load were transferred into the moment frames. Failure index values of the brace cores also decreased as the loads moved away from the BRBF plane. This confirms that the most conservative BRBF design method for ULCF involves designing BRBFs to withstand direct lateral loading.

Torsion in the hinged BRBF beams created stress increases at the end of the upper gusset-to-beam connections. The stress increase was not large enough to cause yielding; however, beam torsion may become a critical failure mode under more severe ground motions. The torsion in the beams was most likely created from the eccentricity between the brace connection to the bottom flange of the beam and the slab constraint at the top flange.

4.3 RECOMMENDATIONS

It is recommended that full-scale testing be conducted to explore the interaction between the concrete slab and the BRBF beams and columns, to validate the rigid slab predictions. With a greater knowledge of the slab constraints, further analytical models can be developed to better investigate splice plate system-level performance. Also to better assess BRBF connection response to out-of-plane loadings, further analysis should be conducted using two orthogonal acceleration records and varied building orientations. Because the drifts in this study were minor, additional analysis with more severe ground accelerations may yield useful post-elastic splice plate results.

REFERENCES

ASCE (2005). "Minimum Design Loads for Buildings and Other Structures." ASCE/SEI 7-05, American Society of Civil Engineers, Reston, VA.

Black, C. J., Makris, N., and Aiken, I. D. (2004). "Component testing, seismic evaluation and characterization of buckling-restrained braces." *J. of Struct. Eng.*, 130(6), 880-894.

Chi, W.-M., Kanvinde, A. M., and Deierlein, G. G. (2006). "Prediction of ductile fracture in steel connections using SMCS criterion." *J. of Struct. Eng.*, 132(2), 171-181.

Coy, B. B. (2007). "Buckling-restrained brace connection design and testing." masters thesis, Brigham Young University, Provo, UT.

Fahnestock, L.A., Ricles, J.M, and Sause, R. (2007). "Experimental evaluation of a large-scale buckling-restrained braced frame", *J. of Struct. Eng.*, 133(9), 1205-1214.

Fell, B. V., Myers, A. T., Deierlein, G. G., and Kanvinde, A. M. (2006). "Testing and simulation of ultra-low cycle fatigue and fracture in steel braces." Proceedings of the 8th U.S. National Conference on Earthquake Engineering, San Francisco, CA, Paper No. 587.

Gupta, A., Krawinkler, H. (1999). "Prediction of seismic demands for SMRFs with ductile connections and elements." *Report No. SAC/BD-99/06*, SAC Joint Venture, Sacramento, CA.

Hancock, J. W., and Mackenzie, A. C. (1976). "On the mechanics of ductile failure in high-strength steel subjected to multi-axial stress-states." *J. Mech. Phys. Solids.*, 24(3), 147-160.

HKS (2006). *ABAQUS Standard Users Manu, Version 6.4l*, Hibbitt, Karlsson, and Sorensen, Inc., Providence, RI.

Inoue, K., Sawaizumi, S., and Higashibata, Y. (2001). "Stiffening requirements for unbonded braces encased in concrete panels." *J.l of Struct. Eng.*, 127(6), 712-720.

Koh, C. G., Ang, K. K., and Chan, P. F. (2003). "Dynamic analysis of shell structures with applications to blast resistant doors." *Shock and Vibration,* 10, 269-279.

Ricles, J. M., Fahnestock, L. A., and Sause, R. (2007). "Studies of earthquake-resistant buckling restrained braced frame systems." *Proceedings of the North American Steel Construction Conference,* AISC, New Orleans, LA, April 2007.

Richards, P. W., and Prinz, G. S. (2007). "Nonlinear time-history analysis of refined mesh steel structures." Proceedings of the 9th Canadian Conference on Earthquake Engineering, Ontario, Canada, Paper No. 1365.

Richards, P.W., Ruiz-Garcia, J., and Uang, C-M., 2002. "Cyclic testing of deep-column RBS steel moment connections for Providence Saint Joseph Medical Center." *Report No. TR-2002/05*, Department of Structural Engineering, University of California at San Diego, La Jolla, CA.

Roeder, C. W., Lehman, D. E., Christopulos, A. (2006). "Seismic performance of special concentrically braced frames with buckling restrained braces." Proceedings of the 8th U.S. National Conference on Earthquake Engineering, San Francisco, CA, Paper No. 1503.

Sabelli, R., Mahin, S., and Chang, C. (2003). "Seismic demands on steel braced frame buildings with buckling-restrained braces", Elsevier Science Ltd., *Engineering Structures*, 25 (2003), 655-666

SAC Joint Venture, 2000. "Recommended seismic design criteria for new steel moment-frame buildings," prepared by the SAC Joint Venture for the Federal Emergency Management Agency, *Rep No.FEMA-350,* FEMA, Washington D.C.

Shahkarami, A. and Vaziri, R. (2007). "A continuum shell finite element model for impact simulation of woven fabrics." *Int. J. Impact Eng.,* 34(1), 104-116.

Tremblay, R., Bolduc, P., Neville, R., and DeVall, R. (2006). "Seismic testing and performance of buckling-restrained bracing systems" *Canadian J.l of Struct. Eng.,* 33, 183-198.

Walters, M. T., Maxwell, B. H., and Berkowitz, R. A. (2004). "Design for improved performance of buckling-restrained braced frames." *SEAOC 2004 Convention proceedings*, 506-513.

Appendix A. VALIDATION OF FATIGUE MODEL

A.1 INTRODUCTION

Ultra-low cycle fatigue (ULCF) fracture is the ductile fracture of materials subject to large plastic strains. ULCF is a governing mode of failure in ductile steel systems.

The development of ultra-low cycle fatigue (ULCF) criterion over the past 30 years has led to a proven fracture prediction method based on material micromechanics. Using void growth rates and combinations of stress and strain states, Hancock and Mackenzie (1976) developed a critical strain parameter to predict void coalescence into macroscopic fractures. The critical strain parameter led to the creation of a micromechanics based stress modified critical strain (SMCS) criterion, whereby conditions for ductile fracture initiation could be evaluated (Chi et al., 2004).

Fell et al. (2006) used the SMCS criterion in the creation of an ULCF failure index relating strain capacities and demands whereby fatigue failure could be determined. For validation of this methodology, a detailed finite element model of a special concentrically braced frame (SCBF) brace was compared to a full scale specimen of identical geometry. The analytical model was created using solid elements and the commercial finite element program ABAQUS (HKS, 2006) was used for the analysis. The ABAQUS test indicated a crack initiation location that was identical to that of the full-scale experiment (Fell et al., 2006).

Following the Northridge earthquake in 1994, inspections of several moment frame connections showed severe damage including brittle fractures at the beam column interface (SAC, 2000). Using the damage data gathered from the seismic event, engineers developed a method of reducing the beam flange cross-section to minimize the

stress concentrations at the connection. Full scale testing of reduced beam section (RBS) connections was conducted at UCSD to investigate the impact of deep columns on connection performance (Richards et al., 2002).

The aim of this section is to provide further validation of the ULCF fracture prediction methodology with the use of shell elements rather than solid elements. By being able to accurately predict fracture initiation in steel specimens, the determination of failure limit states of the buckling-restrained brace frame (BRBF) and moment frame systems in the 3-story directional loading study will be greatly improved.

A.2 EXPERIMENTAL SETUP

Although references are made accordingly, the author of this paper wishes to emphasize that the full scale test specimen described in this section was designed, constructed, and tested by others at the University of California at San Diego (Richards et al., 2002).

A.2.1 Full-Scale Specimen

Results from a full-scale special moment frame deep column failure test, performed by others at UCSD, are compared with results from an ABAQUS finite element model. The detail of the RBS cut used in the full-scale comparison test is given below in Figure A-2. Geometric properties for both the beam and column, along with the connection and actuator locations of the performed experiment are given in Figure A-1. The beam is a W40×183 section and the column is a W36×527 (Richards et al., 2002).

A.2.2 Loading Protocol

The ATC-24 loading protocol used in the experimental testing is controlled by the yield displacement δ_y which was determined to be 1” from material coupon testing (Richards et al., 2002). The loading involves three cycles each at 0.5”, 0.7”, 1”, 2”, 3” continued by two cycles applied at 4”, 5”, 6”, etc, until failure (see Figure A-3 for protocol plot). The same protocol was used for the finite element analysis.

A.3 ABAQUS MODEL

A.3.1 Boundary Conditions & Output Data

To simulate the conditions used in the full-scale experiment, the top and bottom of the column were pinned in the model (see Figure A-4) and rotations of the column and beam were restricted to the plane of the model. Near the beginning of the RBS cut, an out-of-plane displacement condition was also specified to simulate the restraining action of the horizontal supports present in the experiment. A displacement boundary condition was specified at the tip of the beam simulating the same loading protocol as in the full-scale experiment.

Von Mises stresses (S-Mises in ABAQUS), principal stresses (SP in ABAQUS), and equivalent plastic strain (PEEQ in ABAQUS) were selected as output from the center of the RBS region where failure occurred in the experimental testing. Within this region, the mesh was refined to ¼" elements for improved accuracy. Equivalent plastic strain is defined using the plastic strain rate tensor $\dot{\varepsilon}_{ij}^{P}$ in the equation:

$$\text{PEEQ} = \int_0^t \sqrt{\frac{2}{3}\dot{\varepsilon}_{ij}^{P}\dot{\varepsilon}_{ij}^{P}}\,dt \qquad \textbf{(A. 1)}$$

A.3.2 Material Properties

Both the beam and column were taken as A992 steel (Richards et al., 2002) with a bilinear yield curve and non-linear kinematic hardening. The kinematic hardening in the ABAQUS model uses a least squares fit regression to determine C and γ in the equation:

$$\alpha' = \frac{C}{\gamma}\left(1 - e^{-\gamma\varepsilon^{pl}}\right) + \alpha_1 e^{-\gamma\varepsilon^{pl}} \qquad \textbf{(A. 2)}$$

(HKS, 2006), where C is the initial kinematic hardening slope, α',γ, and ε^{pl} are material coefficients obtained from testing, α_1 is the backstress, and γ is the curve rate of departure

from C. For the purposes of this study, parameter values α', γ, and ε^{pl}, determined from material testing, were 63.5, 406.18, and 37.175 respectively.

A.4 FAILURE INDEX

The failure index used to predict low-cycle ductile fracture is determined by dividing equivalent plastic strain (PEEQ) with a critical plastic strain obtained using a stress modified critical strain (SMCS) criterion. The critical plastic strain is taken as:

$$\varepsilon_{p_{CRITICAL}} = \alpha \cdot \exp\left[-1.5 \cdot \frac{\sigma_m}{\sigma_e}\right] \quad \text{(A. 3)}$$

(Hancock and Mackenzie 1976) where σ_m is the mean stress, σ_e is the effective or von Mises stress, and α is a material constant obtained from coupon testing. For the purpose of this study, α is considered to be 2.6 (Chi et al. 2006).

When the equivalent plastic strain exceeds the critical value $\varepsilon_{P|CRITICAL}$, fracture initiation begins; thus, a failure index greater than 1 indicates fracture initiation. The failure index uses ABAQUS output of stresses and strains acquired from the fracture critical location. The critical location for ultra-low cycle fatigue failure was determined from noticeably large plastic strain (PEEQ) accumulations at the center of the reduced beam section cut (Figure A-5).

A.5 COMPARISON OF RESULTS

Hysteretic plots of force vs. displacement for the ABAQUS model and experiment are shown in Figure A-6 and Figure A-7 respectively. From the two plots, similar elastic and plastic behavior can be observed. The deformed configuration of the ABAQUS model showed inelastic buckling near the center of the RBS which corresponds to reductions in strength beginning at a beam tip deflection of four inches (Figure A-6). This corresponds well with the observed and recorded response of the

experimental specimen (Figure A-7). Within the loading cycles, both hysteretic plots indicate similar maximum loads.

ABAQUS output obtained from the critical RBS location indicates a failure index greater than the critical value of 1 during the middle of the 5 inch loading cycle. The full scale test experienced low-cycle fatigue cracks during the 7" loading cycle (Richards et al., 2002). The failure index proves to be conservative by predicting fracture initiation before it actually occurs. The conservative nature of the failure index has been observed in other validation studies (Kanvinde, A. M. and Deierlein, G. G., 2007). A plot of the failure index at each step in the analysis is shown in Figure A-8.

A.6 CONCLUSION

In this validation study experimental results, obtained by others, for a steel moment frame connection are compared with a three-dimensional ABAQUS finite element model incorporating an ULCF criterion. The purpose was to establish validation of fracture prediction methods.

Hysteretic plots of force vs. deflection indicated similar connection resistance between the ABAQUS model and the actual experiment. Both the model and experiment obtained maximum loads near 300 kips, and showed similar inelastic buckling strength losses. This indicates that the ABAQUS model simulated the global behavior observed in the experimental test. The validation of model behavior allowed for the prediction capabilities of the ULCF failure index methodology to be investigated.

Stress and strain values for the failure index were taken from the center of the reduced beam section cut. Here noticeably large plastic strain (PEEQ) accumulations were observed in the experiment. The failure index exceeded the critical value of 1, four loading cycles before fracture of the full-scale experiment. The premature fracture prediction shows that the failure index value is conservative. In instances where the failure index exceeds 1, it is reasonable to say that ULCF fracture is near; and, for indexes less than 1 the absence of fatigue fracture is certain. Thus the failure index is a reasonable prediction for impending fracture and an upper bound for indicating the absence of fracture.

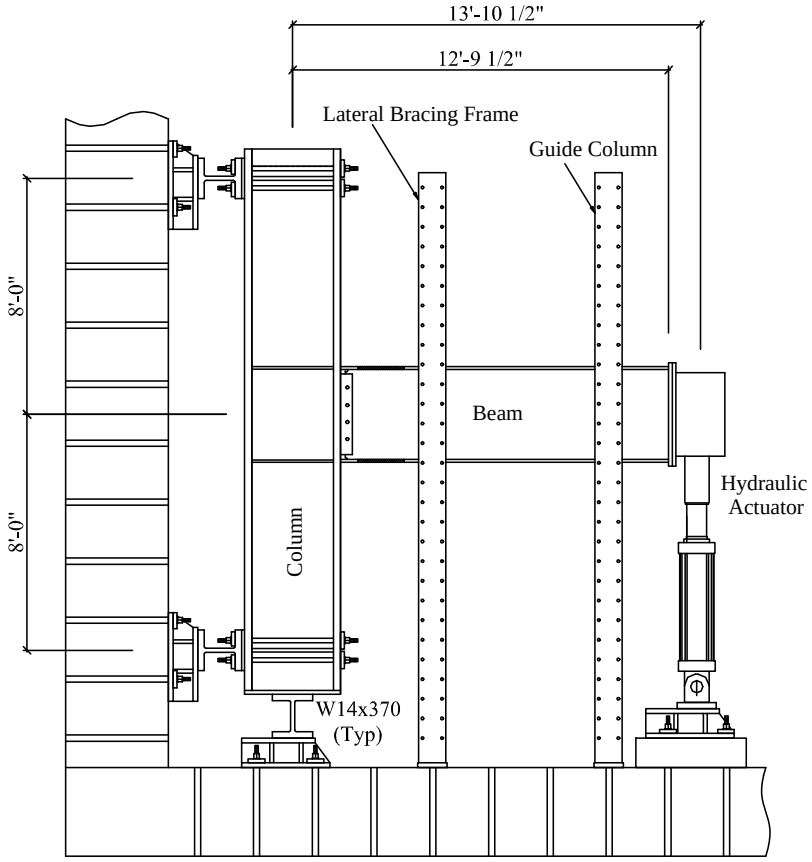

Figure A-1 Test specimen geometry (Richards et al., 2002)

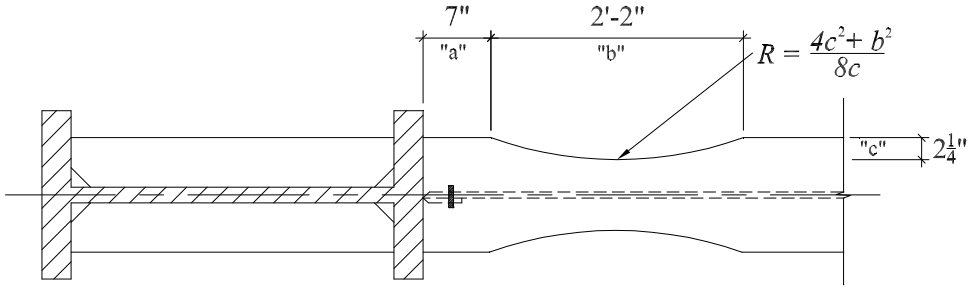

Figure A-2 RBS cut detail (Richards et al, 2002)

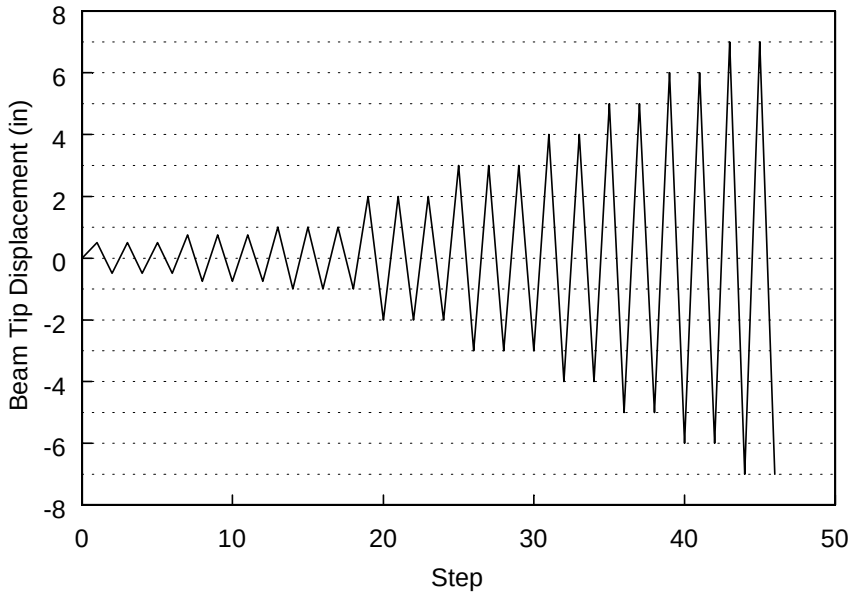

Figure A-3 ATC-24 loading protocol (Richards et al., 2002)

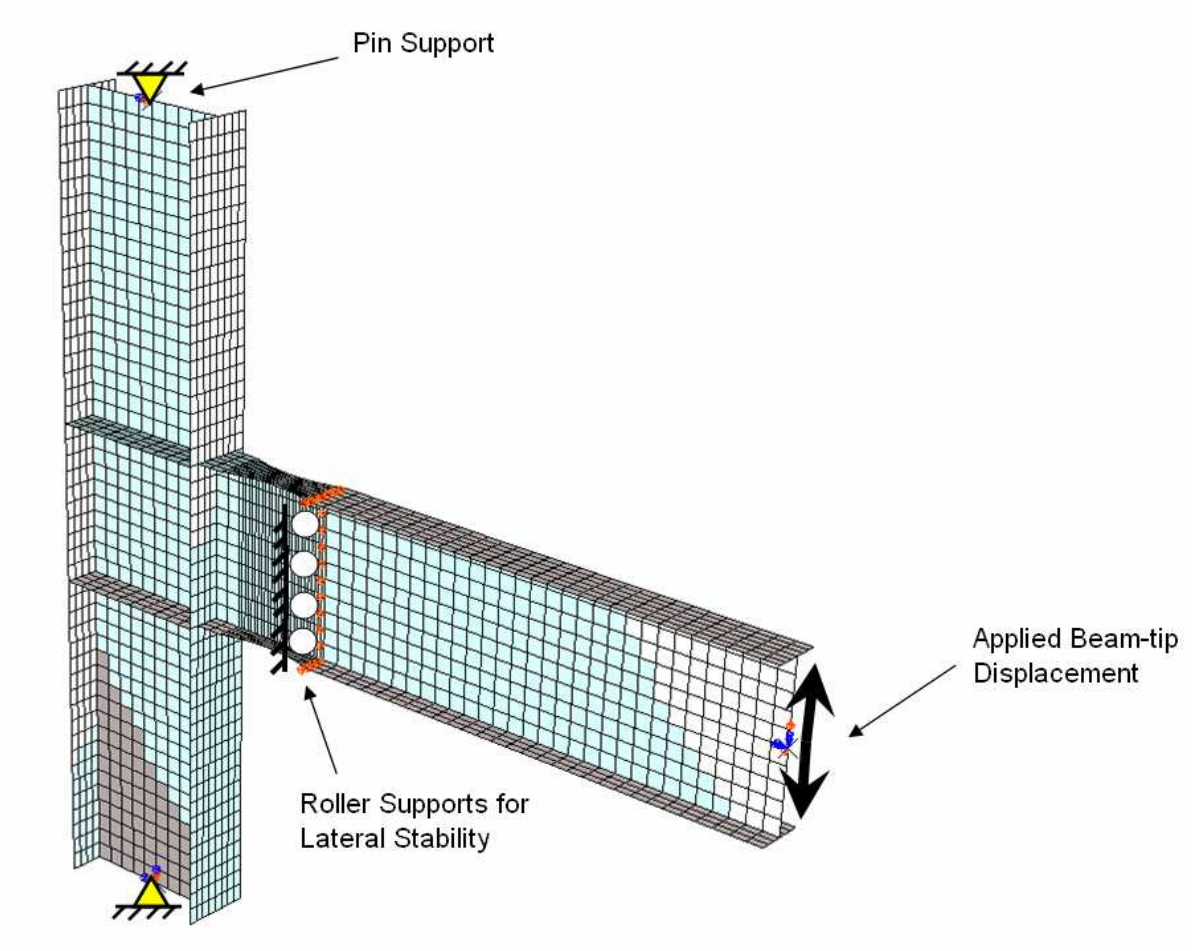

Figure A-4 Refined mesh model with boundary conditions

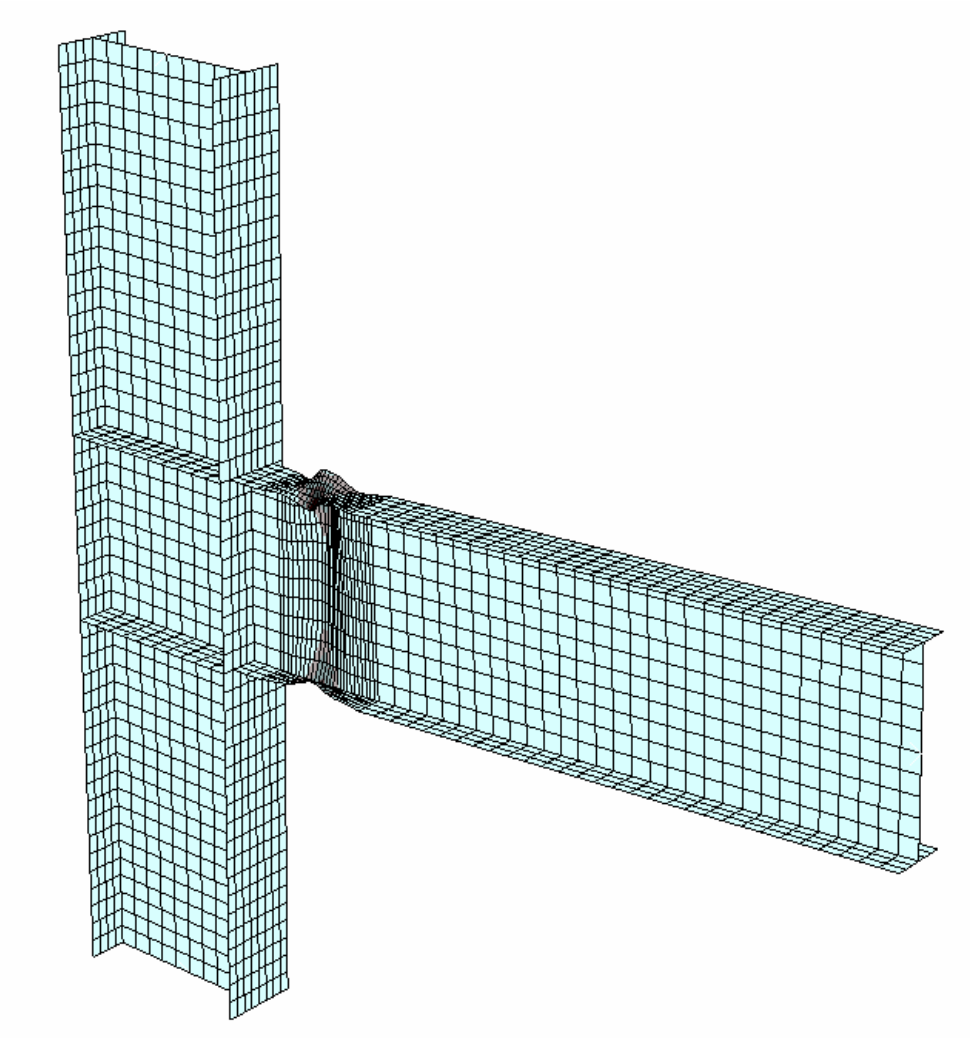

Figure A-5 Cumulative plastic strain and deformed shape at end of loading protocol

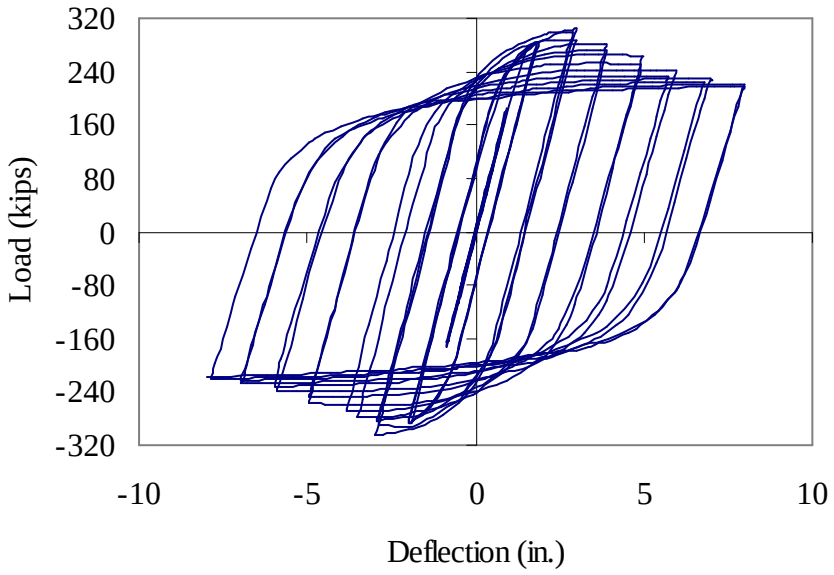

Figure A-6 ABAQUS hysteresis

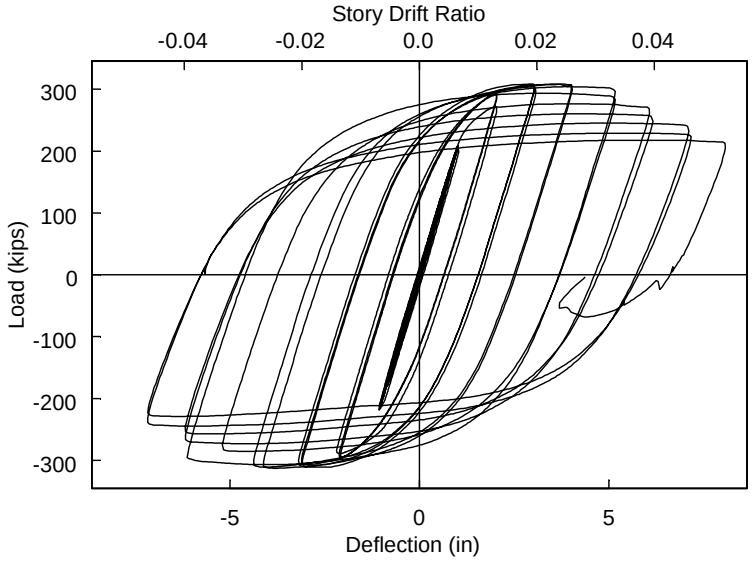

Figure A-7 Experiment hysteresis (Richards et al., 2002)

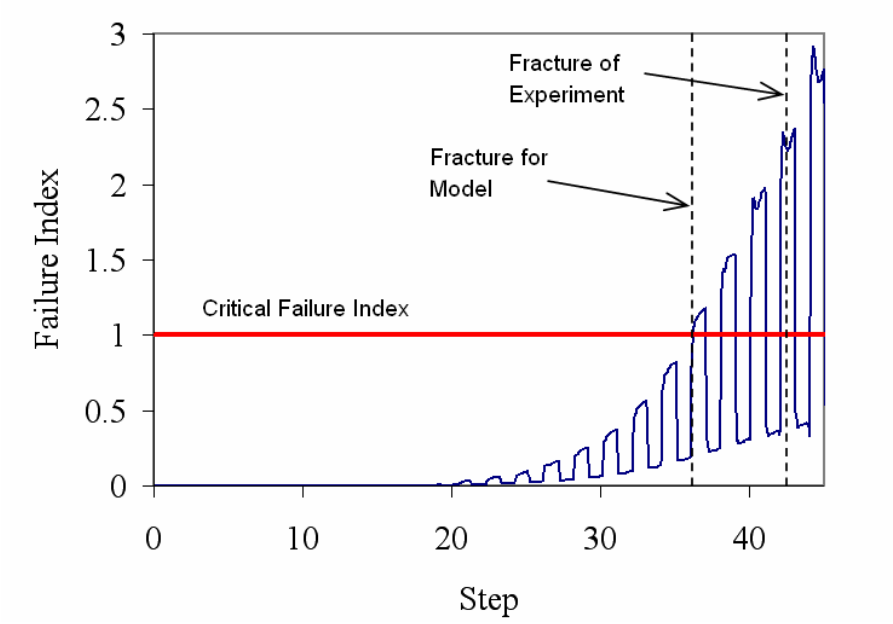

Figure A-8 Failure Index

Appendix B. SEISMIC DESIGN CALCULATIONS

B.1 INTRODUCTION

The following section presents calculations for special moment frames and buckling restrained braced frames (BRBF) designed according to the AISC seismic provisions.

The seismic systems were designed for a three story building utilizing both BRBFs and special moment frames. Utilizing symmetry, one quarter of the building's seismic system is considered in this study. The lateral force resisting bay dimensions and floor masses were taken from a SAC study (Gupta and Krawinkler, 1999) (see Figure B-1). The location and configuration of the BRBFs and special moment frames is also shown in Figure 2-2. The seismic weight for the entire three story building is 6,503 kips. Design values S_{DS} and S_{D1} obtained from a Los Angeles, California building site are 1.120 and 0.606 respectively. Figure B-2 shows the design response spectra.

B.2 SPECIAL MOMENT FRAME DESIGN

The special moment frame design followed the seismic guidelines outlined in ASCE-07 (ASCE, 2005). Member sizes for the special moment frame bays were governed by drift requirements imposed by the design code. Reduced beam section (RBS) moment connections (common in post Northridge moment frames) were included in the design (see Section B.3 RBS CUTS). The detailed moment frame calculations are presented below.

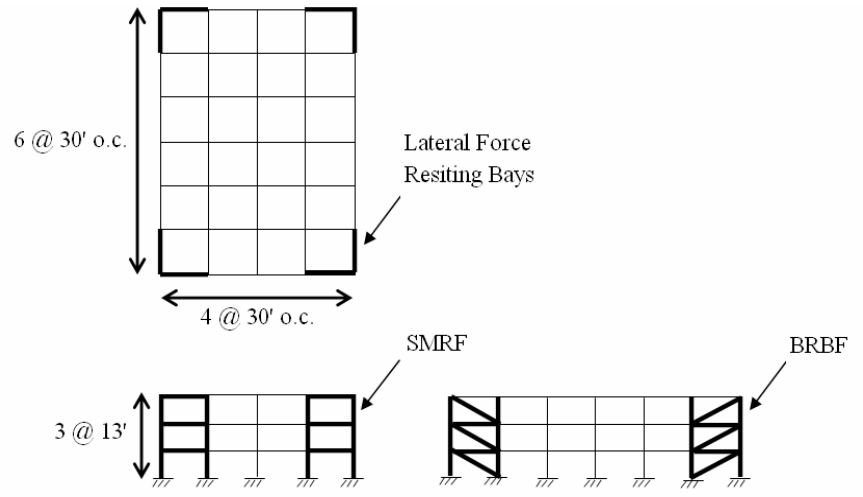

Figure B-1 Plan and elevation view of 3-story building

B.2.1 Calculations

Table B-1: Given Design Loads

Roof (D)	83 psf
Floor (D)	86 psf
Wall (D)	25 psf

Design period:

$$T = Cu \cdot Ta \qquad \text{(B.1)}$$

where: Cu = 1.4 (Table 12.8-1, ASCE 7-05)

$Ta = C_t \cdot h_n^x$

$C_t = 0.028$, $x = 0.8$ (Table 12.8-2, ASCE 7-05)

$Ta = 0.028(39')^{0.8} = 0.5248\,\text{sec}$

$T = 1.4\,(0.5248) = 0.7347\,\text{sec}$

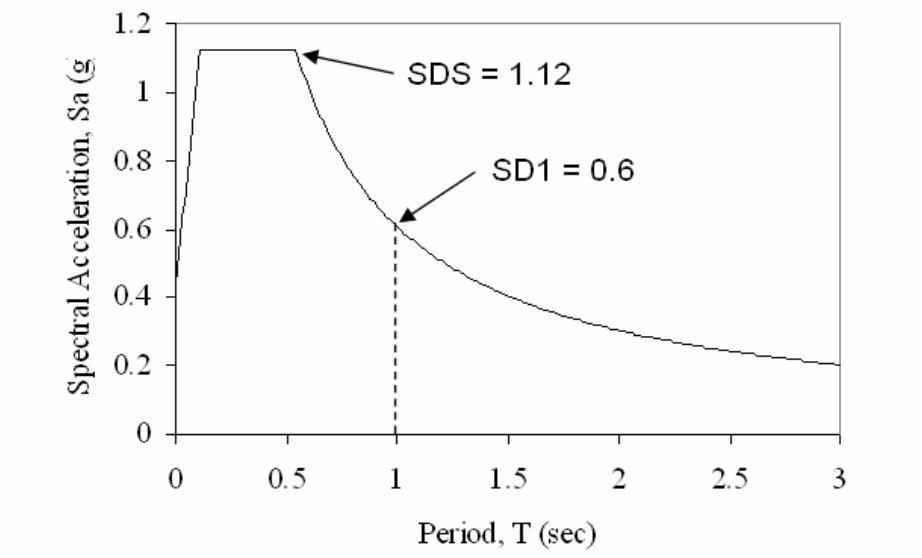

Figure B-2 Design response spectra

Spectral acceleration:

From Figure B-2 using T = 0.7347

SA = 0.8

Base shear:

$$V_B = C_S \cdot W \tag{B.2}$$

where $C_S = \dfrac{S_{DS}}{\left(\frac{R}{I}\right)} = \dfrac{1.12}{\left(\frac{8}{1}\right)} = 0.14$

$$V_B = (0.14) \cdot 6{,}503.112\,\text{k} = 910.4\,\text{k}$$

Distribution of lateral force:

Linear interpolation (12.8.3 ASCE 7-05)

$$K = \frac{1}{2}T + 0.75 = 1.12 \tag{B.3}$$

Table B-2: Lateral Force Distribution on Structure

Floor	W kips	h^K	$W \cdot h^K$	Cvx	F_X kips
1	2110.1	17.69	37,327.7	0.145	132
2	2110.1	38.44	81,112.2	0.316	287
Roof	2282.98	60.53	138,195.7	0.538	489.8
			Σ 256,635.6		

Floors 1 and 2:

Figure B-3 represents a free body diagram (FBD) of floors 1 and 2.

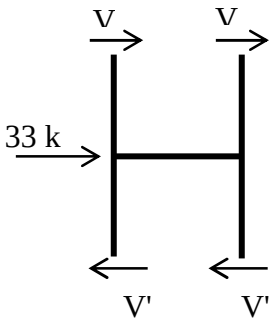

Figure B-3 F.B.D. of floors 1 and 2

$$\sum V = 194.375\,k$$
$$\sum V' = 227.375\,k$$
$$V = 97.19\,k$$
$$V' = 113.69\,k$$

Elastic displacement (Δe):

Assuming $I_{beam} = I_{column}$

$$\Delta e = \frac{(V + V') \cdot h^2}{12 \cdot E}\left(\frac{h}{2 \cdot I} + \frac{L}{I}\right) \qquad \text{(B.4)}$$

$$\Delta e = \frac{(97.19\,k + 113.69\,k) \cdot (13 \times 12\,in)^2}{12(29000\,ksi)}\left(\frac{78\,in + 360\,in}{I}\right)$$

$$\Delta e = \frac{6{,}459.21\,in^5}{I}$$

Allowable elastic displacement (Δae):

$$\Delta ae = \frac{0.025\,h_{SX}}{Cd} \qquad \text{(B.5)}$$

where: Cd = 5.5 (Table 12.2-1 ASCE 7-05)

$$\Delta ae = \frac{0.025(13 \times 12\,in)}{5.5} = 0.7091\,in$$

Required moment of inertia:

$$0.7091\,in = \frac{6{,}459.21\,in^5}{I}$$

$$I_{REQ} = 9{,}109.14\,in^4$$

Chosen members:

W24×279 Columns
W36×160 Beams

Roof:

Figure B-4 represents an FBD of the lateral forces on the roof moment frame.

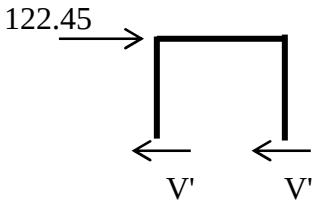

Figure B-4 F.B.D. of Roof

V' = 61.225 k

Elastic displacement (Δe):

$$\Delta e = \frac{(V') \cdot h^2}{12 \cdot E}\left(\frac{h}{2 \cdot I} + \frac{L}{I}\right) \quad \text{(Assuming } I_{beam} = I_{column}\text{)} \qquad \text{(B.6)}$$

$$\Delta e = \frac{(61.225\,\text{k}) \cdot (6.5 \times 12\,\text{in})^2}{12(29000\,\text{ksi})}\left(\frac{39\,\text{in} + 360\,\text{in}}{I}\right)$$

$$\Delta e = \frac{427.08\,\text{in}^5}{I}$$

Allowable elastic displacement (Δae):

$$\Delta ae = \frac{0.025\,h_{SX}}{Cd} \qquad \text{(B.7)}$$

where: Cd = 5.5 (Table 12.2-1 ASCE 7-05)

$$\Delta ae = \frac{0.025(13 \times 12\,\text{in})}{5.5} = 0.7091\,\text{in}$$

Required moment of inertia:

$$0.7091\,\text{in} = \frac{427.08\,\text{in}^5}{I}$$

$$I_{REQ} = 602.3\,\text{in}^4$$

Chosen members:

W24×279 Columns
W27×84 Beams

B.3 RBS CUTS

B.3.1 Calculations for Beams on floors 1 & 2:

Beam section dimensions;

bf = 12” d = 36”

dc = 26.7” tf = 1.02”

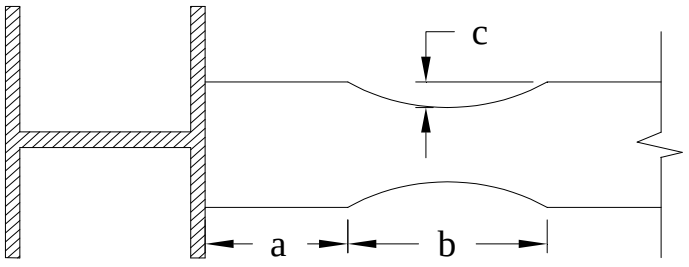

Figure B-5 RBS cut detail

Section properties:

$Zx = 624\ in^3$

Cut dimensions:

$$a = 0.75(bf) \quad \text{(B.8)}$$

$a = 0.75(12) = \underline{9\ in.}$

$$b = 0.85(d) \quad \text{(B.9)}$$

$b = 0.85(36) = 30.6\ in.,\ \underline{USE\ 30.5\ in.}$

$$c = 0.2(bf) \quad \text{(B.10)}$$

$c = 0.2(12) = 2.4\ in.,\ \underline{USE\ 2.5\ in.}$

$$Z_{RBS} = Z_X - (2)(2.5)(tf)(d - tf) \quad \text{(B.11)}$$

$Z_{RBS} = 624\ in4 - (2)(2.5)(1.02\ in.)(36\ in. - 1.02\ in.)$

$Z_{RBS} = 445.6\ in^3$

$$M_F = M_{PR} + V_P(x) \tag{B.12}$$

where: $x = a + \frac{b}{2}$

$$V_P = \frac{M_{PR}}{0.5(L')}$$

$$M_{PR} = C_{PR}(R_Y)(Z_{RBS})(F_Y)$$

From equation B.12, the values of x, M_{PR}, V_P and M_F are as follows:

$$x = 9\,\text{in} + \frac{30.5\,\text{in}}{2} = 24.25\,\text{in}$$

$$M_{PR} = 1.2(1.1)(445.602\,\text{in}^3)(50\,\text{ksi}) = 29409.73\,\text{k - in}$$

$$V_P = \frac{29409.73\,\text{k - in}}{0.5(311.5\,\text{in})} = 188.83\,\text{k}$$

$$M_F = (29409.73\,\text{k - in}) + (188.83\,\text{k}) \cdot (24.25\,\text{in}) = 33{,}988.78\,\text{k - in}$$

Requirement:

$$C_{PR}(R_Y)(Z_X)(F_Y) > M_F \tag{B.13}$$

$$C_{PR}(R_Y)(Z_X)(F_Y) = 1.2(1.1)(624\,\text{in}^3)(50\,\text{ksi}) = 41{,}184\,\text{k - in}$$

Check:

$41{,}184\,\text{k - in} > 33{,}988\,\text{k - in}$ OK

Summary:

a = 9 in.

b = 30.5 in.

c = 2.5 in.

B.3.2 Calculations for Beams on Roof:

Beam section dimensions;

bf = 10” d = 26.7”

dc = 26.7” tf = 0.64”

Section properties:

$Zx = 244\ in^3$

Cut dimensions:

$a = 0.75(bf)$ (B.14)

$a = 0.75(10) = \underline{7.5\ in.}$

$b = 0.85(d)$ (B.15)

$b = 0.85(26.7) = 22.7\ in.,\ \underline{USE\ 22.5\ in.}$

$c = 0.2(bf)$ (B.16)

$c = 0.2(10) = 2\ in.,\ \underline{USE\ 2\ in.}$

Cut dimension calculations continued:

$$Z_{RBS} = Z_X - (2)(2.5)(tf)(d - tf) \quad \text{(B.17)}$$

$$Z_{RBS} = 244\,in^4 - (2)(2.5)(0.64\,in.)(26.7\,in. - 0.64\,in.)$$
$$Z_{RBS} = 177.28\,in^3$$

$$M_F = M_{PR} + V_P(x) \quad \text{(B.18)}$$

where: $x = a + \frac{b}{2}$

$$V_P = \frac{M_{PR}}{0.5(L')}$$
$$M_{PR} = C_{PR}(R_Y)(Z_{RBS})(F_Y)$$

From equation B.18, the values of x, M_{PR}, V_P and M_F are as follows:

$$x = 7.5\,in + \frac{22.5\,in}{2} = 18.75\,in$$
$$M_{PR} = 1.2(1.1)(177.28\,in^3)(50\,ksi) = 11{,}700.45\,k\text{-}in$$
$$V_P = \frac{11{,}700.45\,k\text{-}in}{0.5(322.5\,in)} = 72.56\,k$$
$$M_F = (11{,}700.45\,k\text{-}in) + (72.56\,k)\cdot(18.75\,in) = 13060.95\,k\text{-}in$$

Requirement:

$$C_{PR}(R_Y)(Z_X)(F_Y) > M_F \quad \text{(B.19)}$$

$$C_{PR}(R_Y)(Z_X)(F_Y) = 1.2(1.1)(244\,in^3)(50\,ksi) = 16{,}104\,k\text{-}in$$

Check:

$16{,}104\,\text{k - in} > 13{,}060.95\,\text{k - in}$ OK

Summary:

$a = \underline{7.5\,\text{in.}}$

$b = \underline{22.5\,\text{in.}}$

$c = \underline{2\,\text{in.}}$

B.4 BUCKLING RESTRAINED BRACE FRAME (BRBF) DESIGN

The BRBF bays of the 3-story structure were designed using a capacity based method where the designed brace is taken as the weakest element in the system. This is achieved by designing the beams and columns of each bay to resist ultimate brace forces. The following calculations step through the brace design process using loads given in Table B-1 (Gupta and Krawinkler, 1999).

Roof:

Figure B-6 represents a FBD of the lateral forces on the roof.

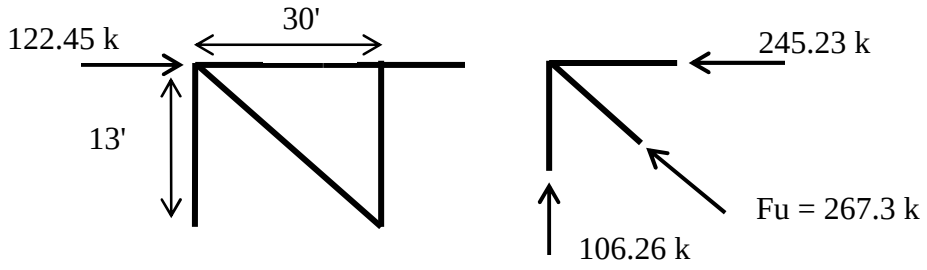

Figure B-6 F.B.D. of BRBF for roof level

Brace Force:

$$F_{BRACE} = 122.45\,k \cdot \left(\frac{32.7'}{30'}\right) = 133.47\,k$$

$$A_{BRACE} = \frac{F_{BRACE}}{\varphi \cdot Fy} \tag{B.20}$$

$$A_{BRACE} = \frac{133.47\,k}{0.9 \cdot (45\,ksi)} = \underline{\underline{3.30\,in^2}}$$

$$F_U = 1.8 \cdot Fy \cdot (A_{BRACE}) \tag{B.21}$$

$$F_U = 1.8(46\,ksi)(3.30\,in^2) = 267.3\,k$$

Floor 2:

Figure B-7 represents an FBD of the lateral forces on floor 2.

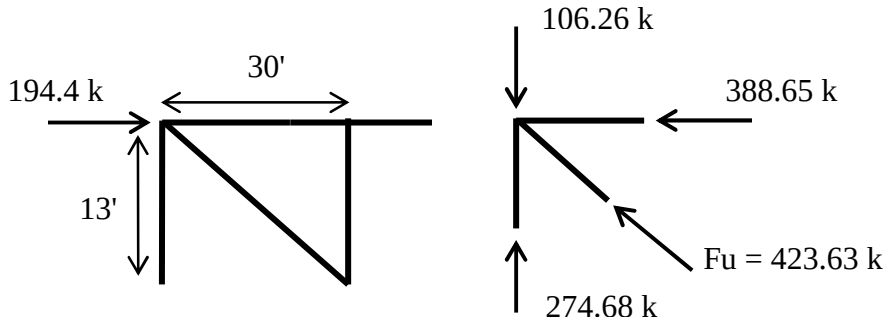

Figure B-7 F.B.D. of BRBF for level 2

Brace Force:

$$F_{BRACE} = 194.4\,k \cdot \left(\frac{32.7'}{30'}\right) = 211.87\,k$$

$$A_{BRACE} = \frac{F_{BRACE}}{\varphi \cdot Fy} \qquad (B.22)$$

$$A_{BRACE} = \frac{211.87\,k}{0.9 \cdot (45\,ksi)} = \underline{\underline{5.23\,in^2}}$$

$$F_U = 1.8 \cdot Fy \cdot (A_{BRACE}) \qquad (B.23)$$

$$F_U = 1.8(46\,ksi)(5.23\,in^2) = 423.63\,k$$

Floor 1:

Figure B-8 represents an FBD of the lateral forces on floor 2.

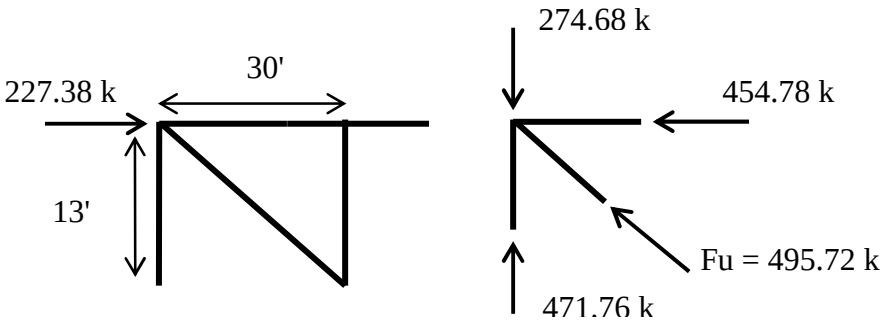

Figure B-8 F.B.D. of BRBF for level 1

Brace Force:

$$F_{BRACE} = 227.375\,k \cdot \left(\frac{32.7'}{30'}\right) = 247.84\,k$$

$$A_{BRACE} = \frac{F_{BRACE}}{\varphi \cdot Fy} \tag{B.24}$$

$$A_{BRACE} = \frac{247.84\,k}{0.9 \cdot (45\,ksi)} = \underline{\underline{6.12\,in}}$$

$$F_U = 1.8 \cdot Fy \cdot (A_{BRACE}) \tag{B.25}$$

$$F_U = 1.8(46\,ksi)(6.12\,in^2) = 495.72\,k$$

B.5 BRBF MEMBERS

B.5.1 Calculation Summary

Table B-3: Column Summary

Floor	Brace Force (kips)	Selected Member	ϕcPn (kips)
1	495.72	W12×53	525
2	423.63	W12×53	525
Roof	267.3	W12×53	525

Table B-4: Beam Summary

Floor	Vmax (k)	Mu (k-ft)	Selected Member	ϕvVn (k)	ϕbMp (k-ft)
1	43.47	326.03	W21×44	217	358
2	43.47	326.03	W21×44	217	358
Roof	32.97	247.28	W21×44[‡]	217	358

[‡] W21×44 is used for construction simplicity, the actual minimum required member is W18×35.

Appendix C. VALIDATION OF MODELING TECHNIQUES FOR SPLICED CONNECTION

C.1 INTRODUCTION

The three story directional loading study incorporates a BRBF connection in which the beam is spliced outside the gusset plate. Lateral forces are transferred through the bolted splice plates. The splices are expected to yield creating hinged regions for increased ductility and protecting critical structural components from damage. Modeling techniques for the connections must be validated to provide confidence in the system model that incorporates them.

To validate the predictive capabilities of the modeling techniques used, a comparison study was performed between an ABAQUS simulation and the results of a full-scale test performed by others at Brigham Young University (Coy, 2007). This comparison study focused on strain values in the splice connector plates.

C.2 EXPERIMENTAL SETUP

C.2.1 Full-Scale Specimen

The experimental test used in this validation study was performed by others at Brigham Young University, Provo. All pertinent figures and results are used with their consent.

C.2.1.1 Geometry& Boundary Conditions

A view of the test setup with self reacting frame is located in Figure C-2. Shown in Figure C-2, the end of the column is pinned to the self reacting frame and actuator motors are attached to the beam tip and brace connector. Each of the four splice connector plates were attached using (9) 7/8" diameter bolts. The dimensions of the gusset plate and brace connection are given in Figure C-1 and Figure C-3 respectively. Geometric properties for the connection test members consist of:

- 4 connector plates (PL 19 ½ x 4 x 5/8)
- W12×72 column (10'-4" length)
- W16×77 beam (40 ¾" length with a 1.5" splice)
- 1" gusset plate

C.2.2 ABAQUS Model

C.2.2.1 Modeling Assumptions

A model of the experiment was developed in ABAQUS using shell elements. The use of shell elements demanded that the connector plates be spaced away from the connecting beam flange. This distance was taken to be the distance between the center of the connector plate and the center of the beam top flange (see Figure C-5). The connecting bolts were modeled using 1-dimensional beam elements with 7/8" diameter bolt area properties.

C.2.2.2 Boundary Conditions & Output Data

Similar to the full-scale experiment, the end of the column was taken to be pinned and loads and displacements were applied to the brace connection and beam end respectively. To restrict the out-of-plane translation of the model, displacement and rotation boundary constraints were applied to the beam and column ends. Figure C-4 shows the applied boundary conditions on the model.

C.2.2.3 Material Properties

Table C-1 shows the material assignments for each of the model components. Bilinear stress-strain curves were used to describe the material behavior for the elastic and plastic range. The ultimate strain for each material in the plastic range was 0.02in./in. and the corresponding stress was f_y+1ksi.

C.2.2.4 Mesh Refinement and Critical Locations

The interest for this study involved the inelastic behavior of the connector plates. The design of such plates is done with the intent that the plates are the critical location in the BRBF system. Because large accumulated plastic strains were expected within the plate region spanning the beam splice, the mesh in this region was refined to 1/5" elements.

C.2.3 Loading Protocol

The static loading of the simulated BRBF consists of an applied force at the end of the brace connection, and an induced horizontal displacement at the top flange of the beam tip. Figure C-6 shows a plot of the applied force per incremental step, and Figure C-7 shows a plot of the induced displacement per incremental step. To simulate frame drifts, these forces and displacements were simultaneously applied at each increment. It is important to note that the force on the brace connection was applied in the line of action of the brace.

C.3 RESULTS AND DISCUSSION

C.3.1 Connector Plate Strain

Strain values obtained from the outer edge of the bottom plates were compared with those recorded during the full-scale experiment. The ABAQUS model predicted a maximum plate strain of 0.012 in./in. and a minimum strain of -0.0056 in./in.. The test recorded a maximum plate strain of 0.011 in./in. and a minimum strain of -0.0052 in./in..

The ABAQUS model strains are within 10% of those recorded in the experiment. Figure C-10 shows strain plots of the ABAQUS model and experimental test respectively. Peak values in the figure do not line up because the ABAQUS model recorded strains independent of strain rate whereas the test did not.

C.3.2 Fatigue Analysis

Localized stress and strain states were incorporated into a stress modified critical strain (SMCS) failure index to determine the occurrence of low-cycle fatigue failure in the top connector plates. It is within this top plate region that the equivalent plastic strain is largest (see Figure C-9).

Figure C-11 shows a plot of the failure index values obtained from the outer edge of the top connector plates. The largest failure index value is 0.872, indicating that the critical value of 1 has not been exceeded and thus fracture initiation of the plates has not occurred.

C.3.3 Gap Rotations

Opening and closing rotations in the ABAQUS model beam splice were compared with the rotations recorded from the full scale test. Rotations from the model were calculated from nodal displacements taken from the upper and lower flanges on either side of the beam splice. The rotation angle was then plotted, with the angle of rotation and resultant beam tip force on the on the abscissa and ordinate axes respectively (see Figure C-12). This was done for easy comparison with the test results which were formatted similarly.

The maximum recorded angle of rotation for the ABAQUS model was 4.91°. The maximum recorded angle of rotation for the test is approximately 7°. The ABAQUS value is within 30% of the maximum recorded gap rotation observed in the test. Figure C-13 shows the gap rotation versus force for the full scale test. Bolt slip in the full scale test may have altered the accuracy of the results. Bolt slip was not incorporated into the ABAQUS model.

C.4 CONCLUSION

To validate the modeling techniques used to simulate the BRBF beam splice connection, splice plate strains obtained from a full scale test specimen were compared with calculated strains from an ABAQUS finite element model. In addition, the advanced predictive capabilities of the ULCF failure index were incorporated into the model to assess the failure critical state of the splice connector plates.

The recorded strains from the ABAQUS model indicated maximum and minimum values within 10% and intermediate peak strains within 15% of those recorded from the experimental strain gauges. With such close prediction of actual plate strains, the modeling assumptions involving the plate to flange spacing, 1-dimensional bolt beam elements and assumed material behavior, used to construct the spliced region are reasonable.

Failure index values obtained from the center of the top connector plates indicated that fracture of the plates had not occurred. In fact, after experiencing drifts in excess of 6 percent, the plates were just over 80 percent of critical damage. The model correctly predicted that fracture had not occurred.

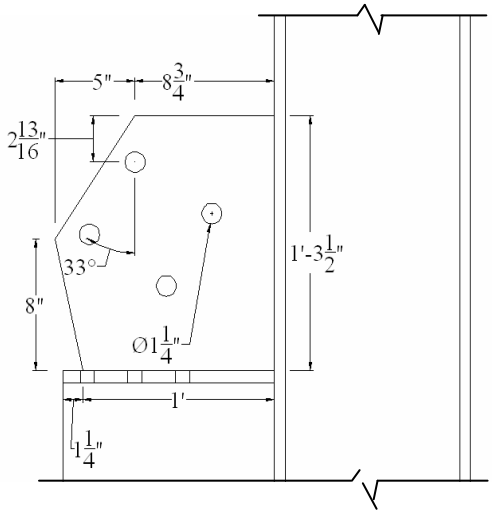

Figure C-1 Gusset plate detail (Coy 2007)

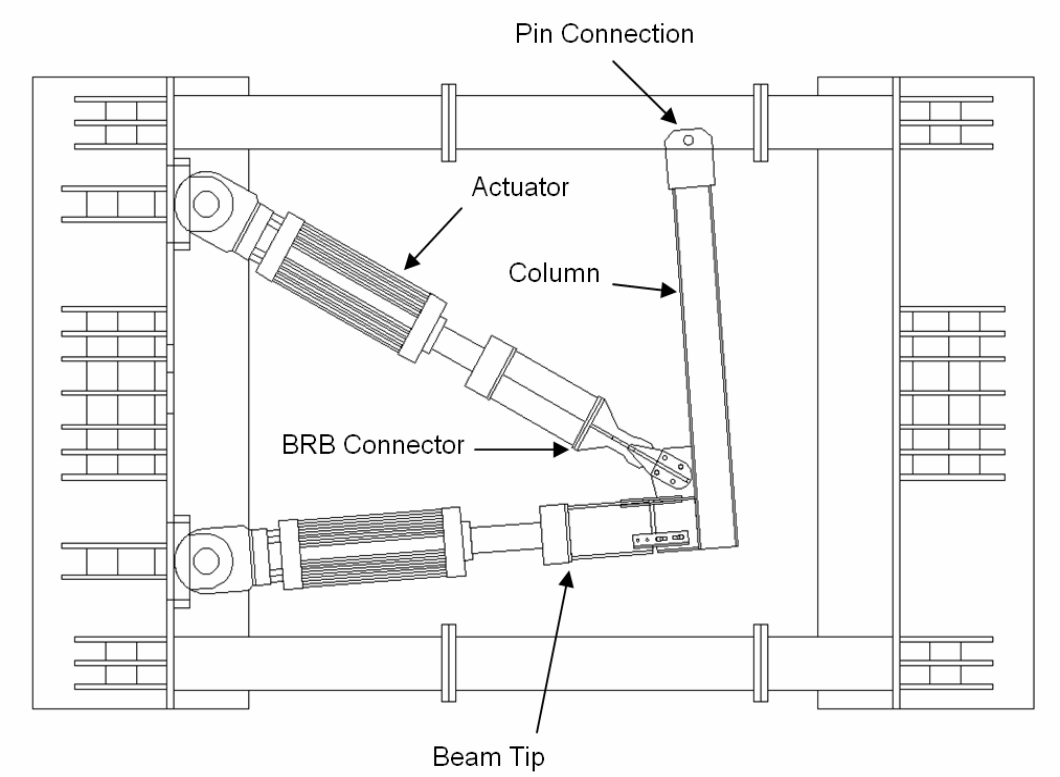

Figure C-2 Experimental setup in self reacting frame (Coy 2007)

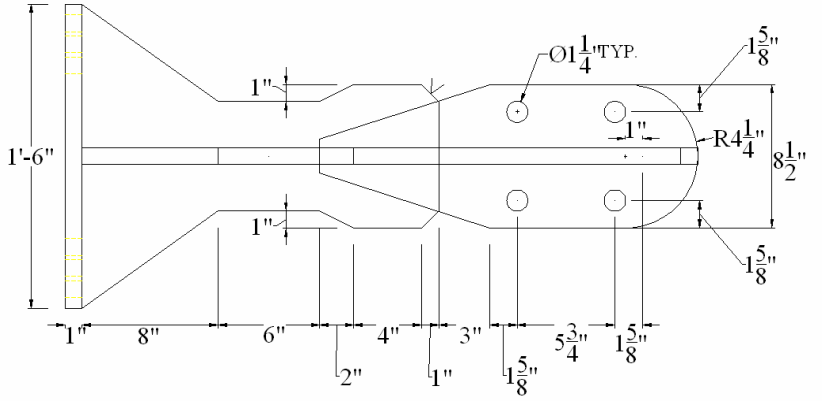

Figure C-3 Brace connection detail (Coy 2007)

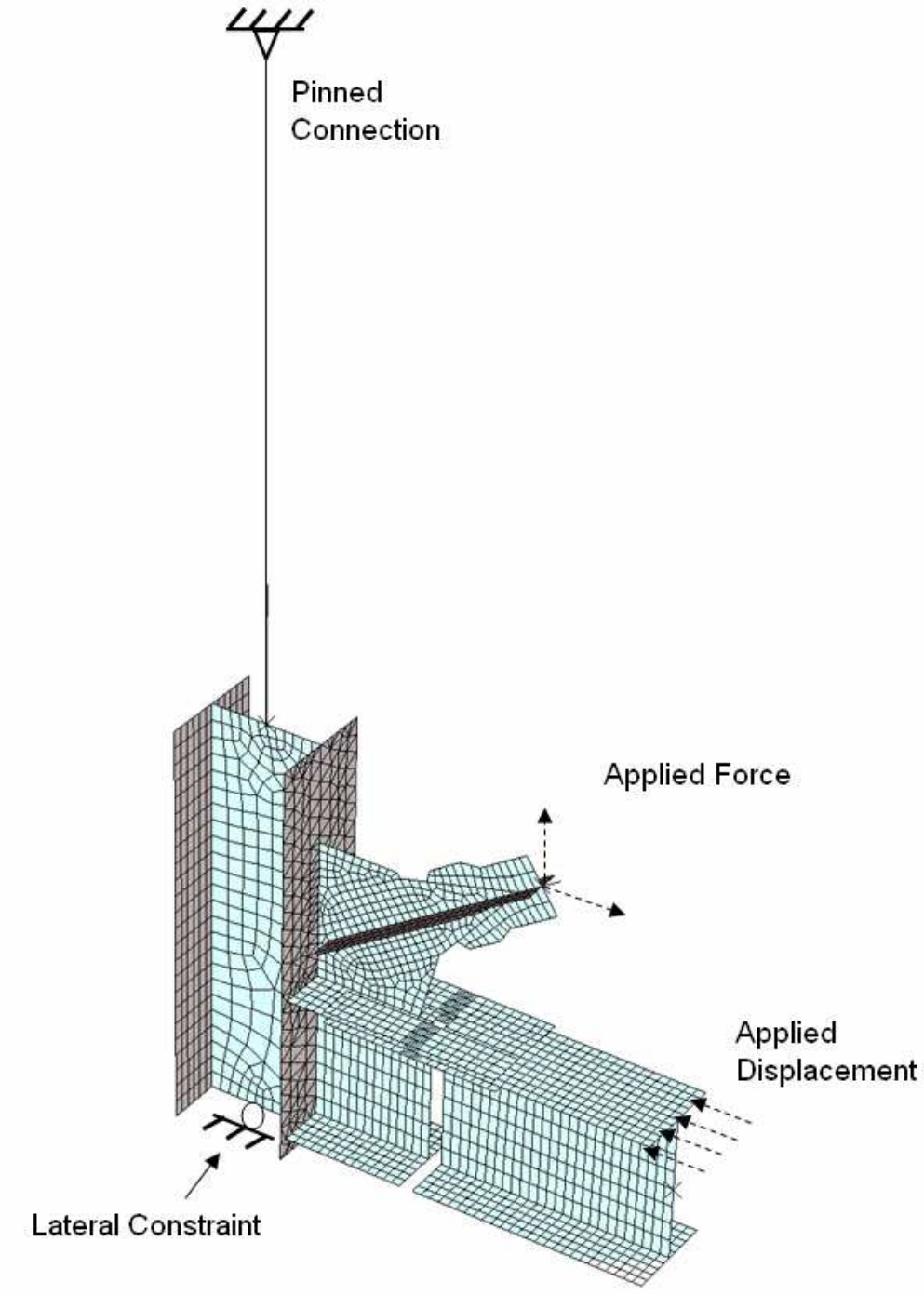

Figure C-4 ABAQUS model boundary conditions and loadings

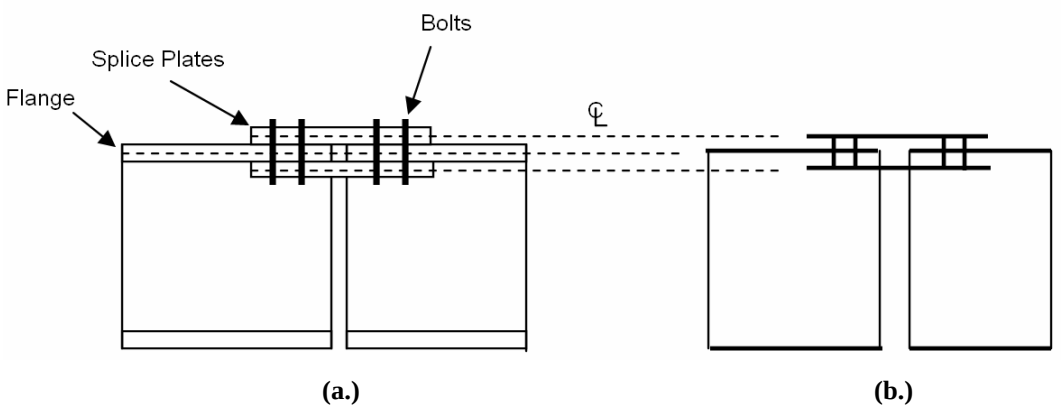

Figure C-5 (a.) Experiment representation; (b.) Shell model representation

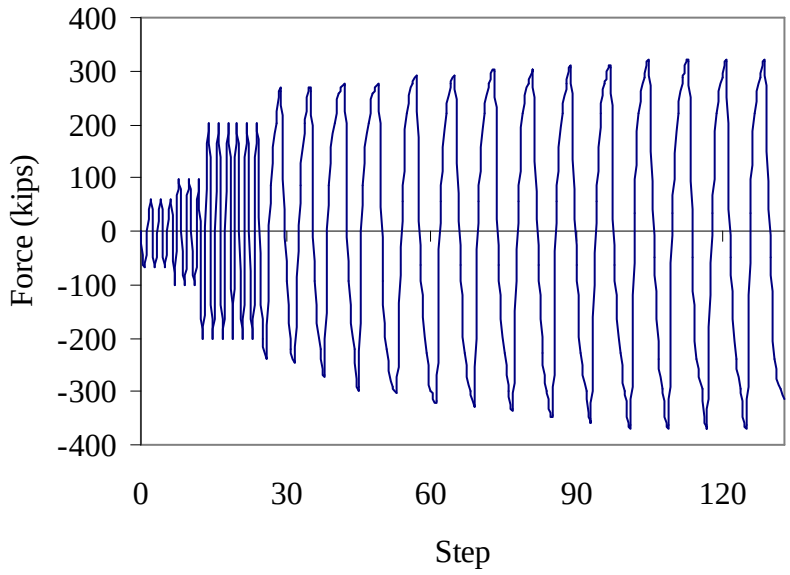

Figure C-6 Force protocol (Coy 2007)

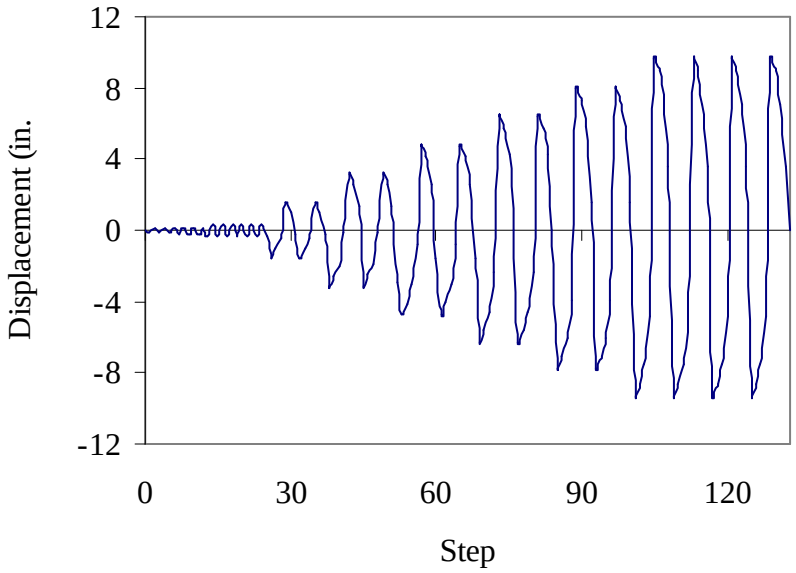

Figure C-7 Displacement protocol (Coy 2007)

Table C-1: Material Assignments.

Part	Steel Type	Fy (ksi)
Column	A992	50
Beam	A992	50
Connector Plates	A36	36
Gusset Plate	A36	36
Brace	A242	46

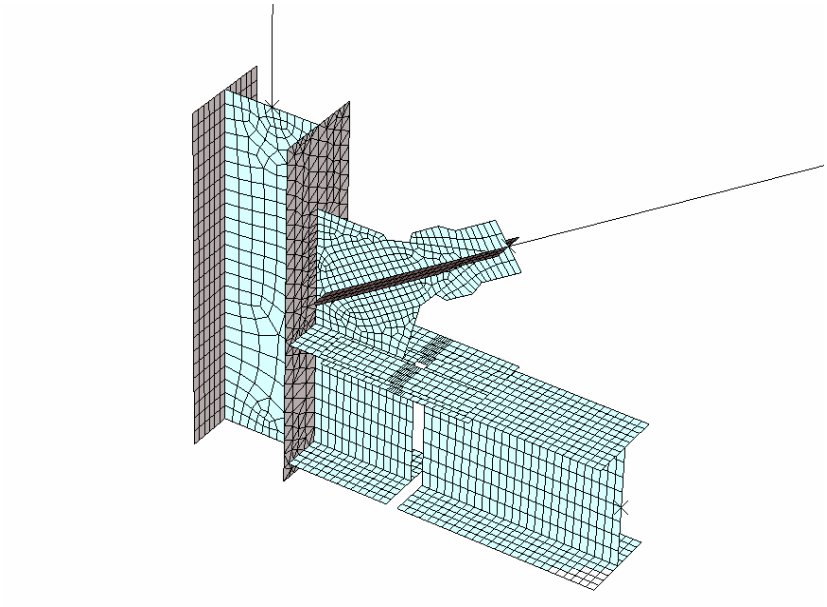

Figure C-8 Refined mesh model

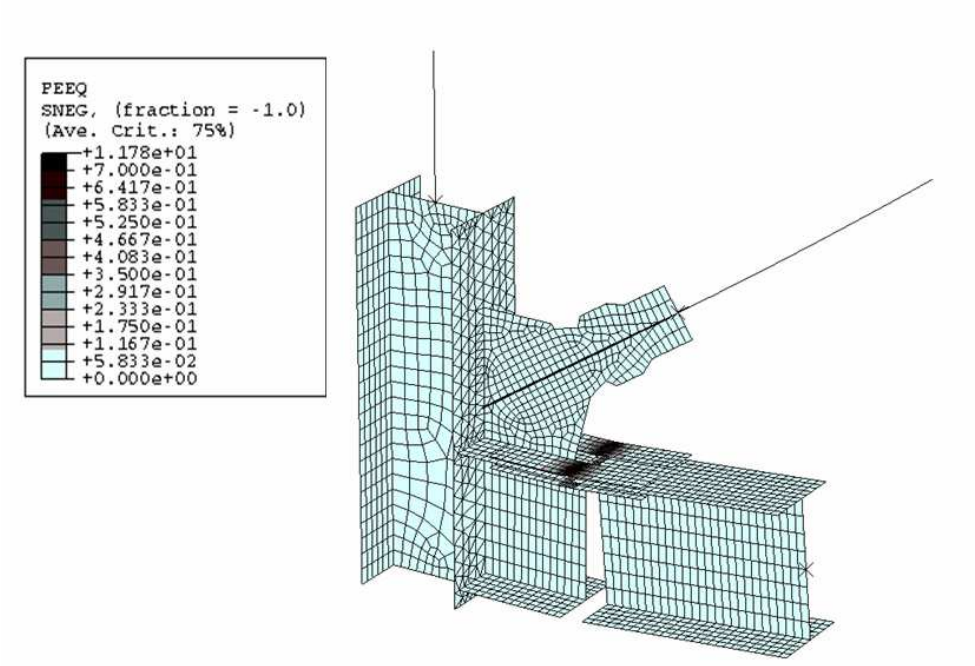

Figure C-9 Plastic strain at center of connector plates

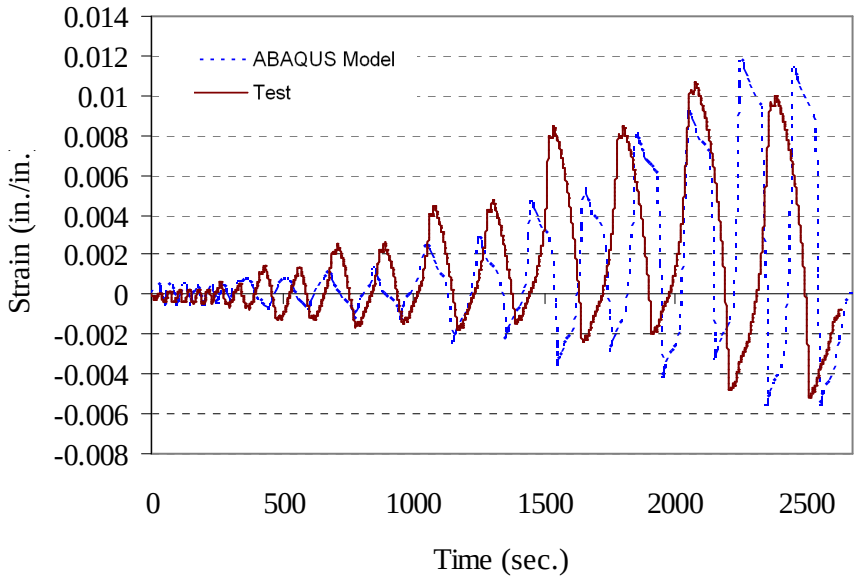

Figure C-10 Strain comparison between ABAQUS model and test (Coy 2007)

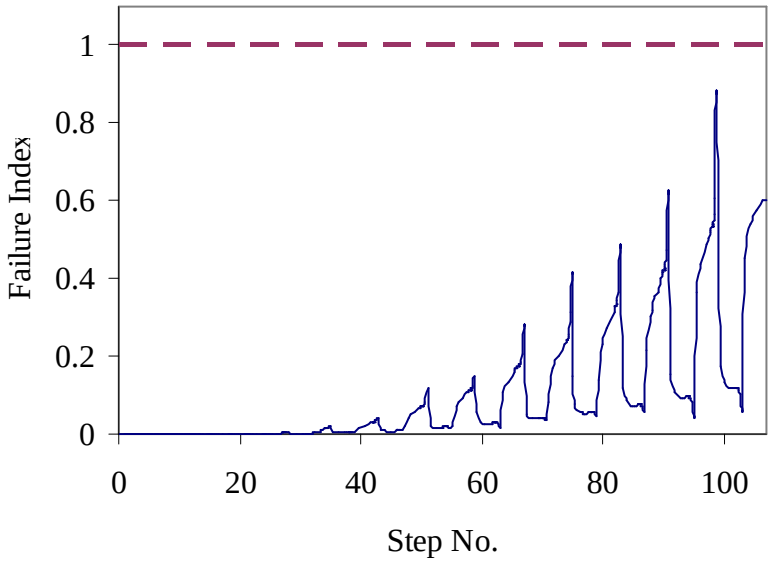

Figure C-11 Failure index of top connector plate

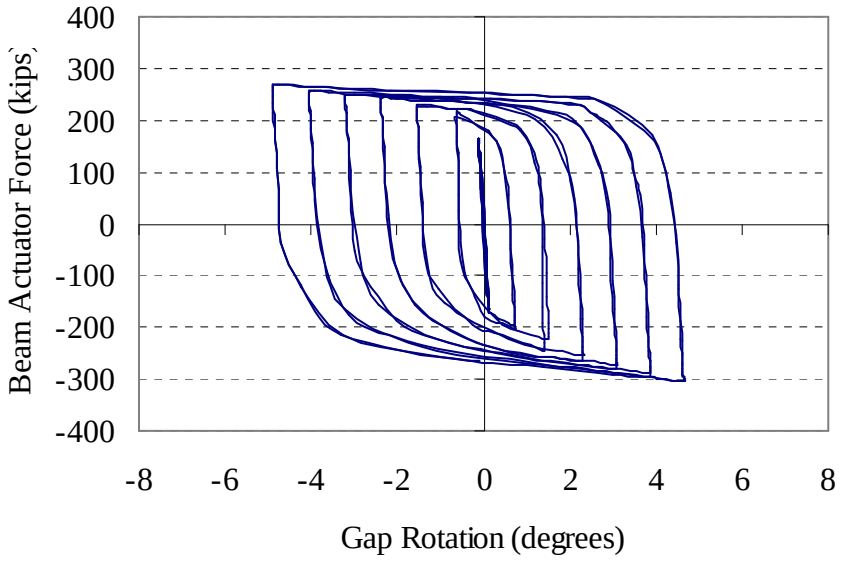

Figure C-12 Gap rotation versus beam actuator force (ABAQUS model)

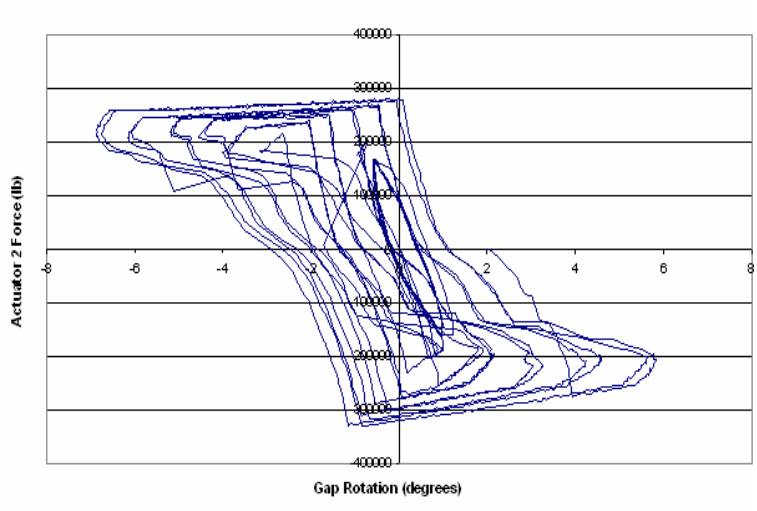

Figure C-13 Gap rotation versus beam actuator force (full scale test)

Appendix D. COMPARING SHELL ELEMENT MODELS WITH BEAM ELEMENT MODELS

D.1 INTRODUCTION

Finite element analysis has become a useful tool in the analysis of complex structures. Structures that otherwise would have required actual construction and testing in a laboratory environment can now be analyzed via a discretized geometry, shape functions, and combinations of constitutive and compatibility equations. To investigate the benefit of using shell elements in connection regions, a comparison study using beam elements will be performed. The shell element analysis will be performed using ABAQUS and the beam element analysis will be performed using Ruaumoko.

The goal of this study is to show that the predictive capabilities associated with the advanced finite element modeling exceed those possible with the simplified 1-dimensional modeling. These advanced predictive capabilities involve the capturing of reduced strength due to yielding and post yield buckling, as well as the determination of localized stress concentrations for low-cycle fracture prediction.

D.2 COMPARISON STUDY

D.2.1 Ruaumoko Model

The 1-D Ruaumoko analysis used in this validation study was not performed by the author, but is described here for comparison with the author's models.

The members of the moment resisting frame are shown in Figure D-1 and a typical detail of the included RBS cut is given in Figure D-2. To model the RBS cut using the 1-D Ruaumoko analysis and to provide sufficient ductility to the frame, regions of lumped plasticity were placed at specific locations as shown in Figure D-3. A seismic mass of 259.3 kN-s^2/m, influencing one moment frame bay, was divided into two parts and placed at the tip of each column as shown in Figure D-3. The base connection of the frame was taken to be pinned.

D.2.2 ABAQUS Model

D.2.2.1 Modeling Assumptions

Figure D-4 shows the modeled moment frame with shell elements in the connection regions, and beam elements in regions where yielding is not expected. The beam elements were inserted to reduce the analysis computational time.

Similar to the Ruaumoko analysis, the base of the moment resisting frame was taken to be pinned, and the specified lumped masses were placed at the tip of each column. The finite element model utilized four-node quadrilateral elements and linear shape functions to discretize the moment frame geometry. A refined mesh with increased nodes was localized at the center of the RBS cut for improved output accuracy. This refined mesh is shown in Figure D-5. In this region, it was assumed that material plastic strain accumulations would be largest.

D.2.2.2 Material Properties

The material for this study was taken to be A992 steel with a yield strength of 50 ksi. Kinematic hardening was used within the ABAQUS analysis. For the kinematic hardening parameters used in the ABAQUS model see Appendix A. Also located in Appendix A is the failure index methodology used for ULCF prediction.

D.2.3 Earthquake Loading

For this study earthquake accelerations recorded from the 1989 Loma Prieta, California, earthquake, were used to load the modeled frame. Figure D-6 represents the

Loma Prieta ground acceleration recorded from Agnews State Hospital in San Jose California. The peak ground acceleration is 0.172g. For this comparison study, two scaled versions of this record were used: the actual record (1x) and a record scaled up 3.366 times to meet the design response spectra (3.366x). Figure D-7 shows superimposed plots of each spectra.

D.4 RESULTS AND DISCUSSION

Figure D-8 shows the roof drift comparison between the Ruaumoko analysis and ABAQUS analysis under the 1x loading protocol. It is noticed in Figure D-8 that both analyses methods show maximum and minimum displacement values of within 10%. Under the 3.366x loading as shown in Figure D-9, the peak drift values of each analysis method remained within 10%.

Figure D-10 shows the failure index over time obtained from the ABAQUS analysis using the 3.366x scaled acceleration spectra. The critical location for ULCF was determined from Figure D-11 which shows large accumulations of plastic strain at the center of the RBS cut. The maximum failure index value is 0.294. This indicates that the beam has not experienced low-cycle ductile fracture, and using Miner's rule it may be inferred that the beam will remain un-fractured following two additional earthquakes of similar magnitude.

D.5 CONCLUSION

The predictive capabilities of the shell element modeling exceeded those possible with the beam element modeling. It was observed that the calculated drifts between the two methods had an error of within 10%. With such close drift results, the use of the computationally expensive advanced finite element analysis cannot be justified; however, it is found that the FEA does offer valuable insight into structural failure limit states which are outside the capabilities of the 1-dimensional analysis. This involves the determination of localized stress and strain data which can be incorporated into a failure index.

The predictive capabilities of the shell element analysis did not indicate failure in the RBS; however, based solely on the drift data from the Ruaumoko model for the 3.366x event, it could be incorrectly concluded that the beam section would fail. This conclusion would be based on experimental testing indicating that RBS sections typically experience failure during drifts of between 4 and 5 percent (Richards et al, 2002).

Figure D-1 Special moment frame members (Richards and Prinz, 2007)

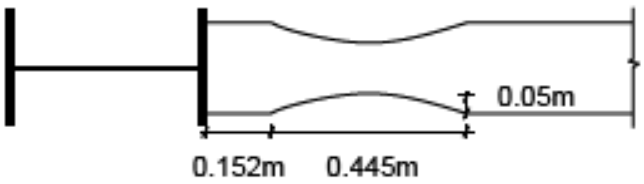

Figure D-2 RBS cut detail (Richards and Prinz, 2007)

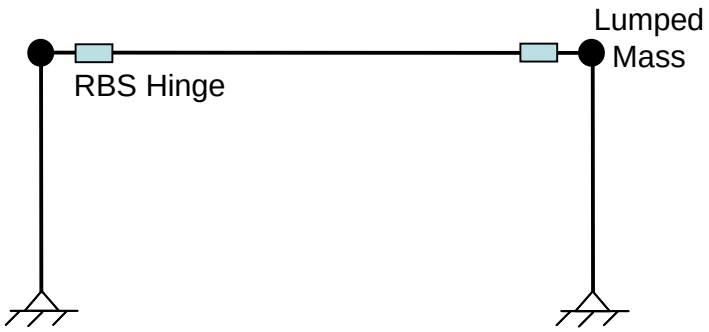

Figure D-3 1-D model with RBS hinge (Richards and Prinz, 2007)

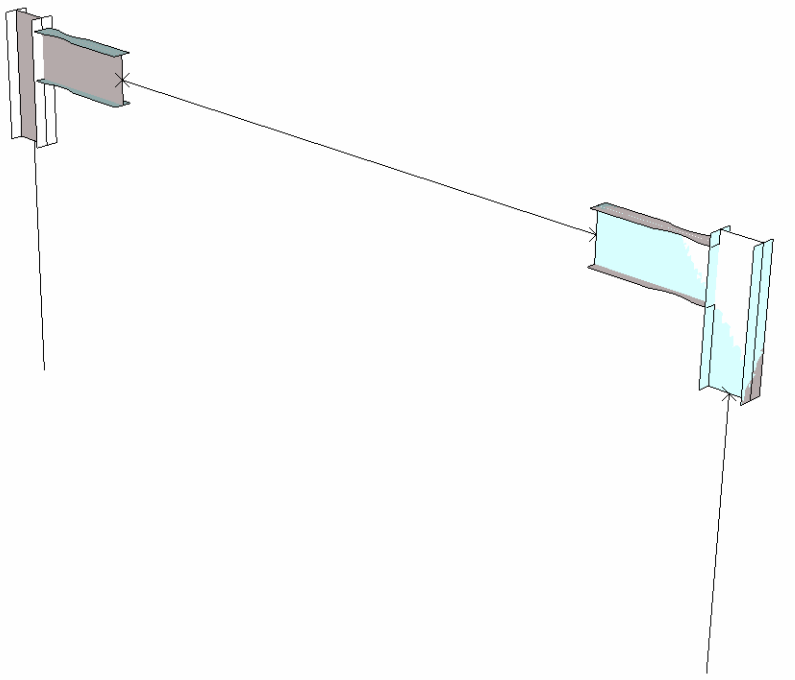

Figure D-4 Modeled moment frame with shell and beam elements

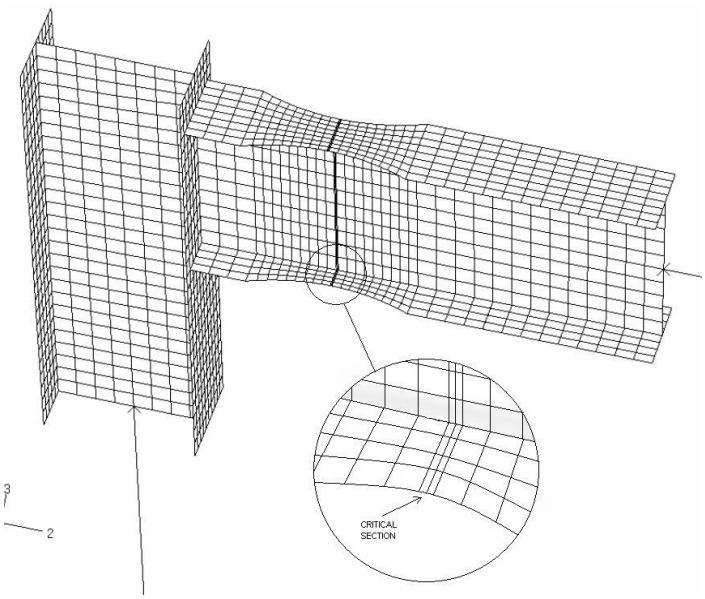

Figure D-5 Refined mesh at RBS

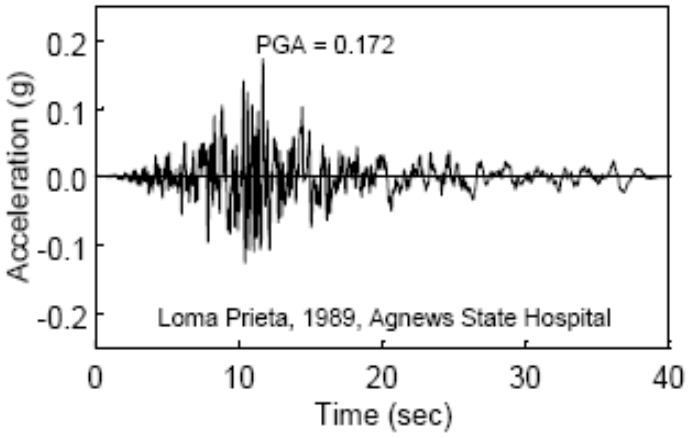

Figure D-6 Earthquake acceleration record (Richards and Prinz, 2007)

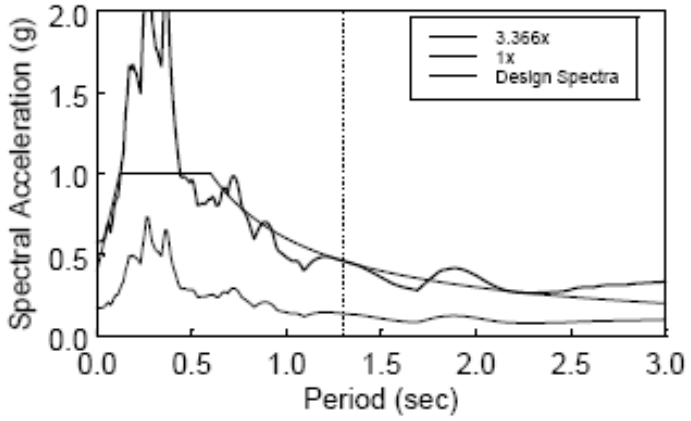

Figure D-7 Spectra for 1x and 3x events (Richards and Prinz, 2007)

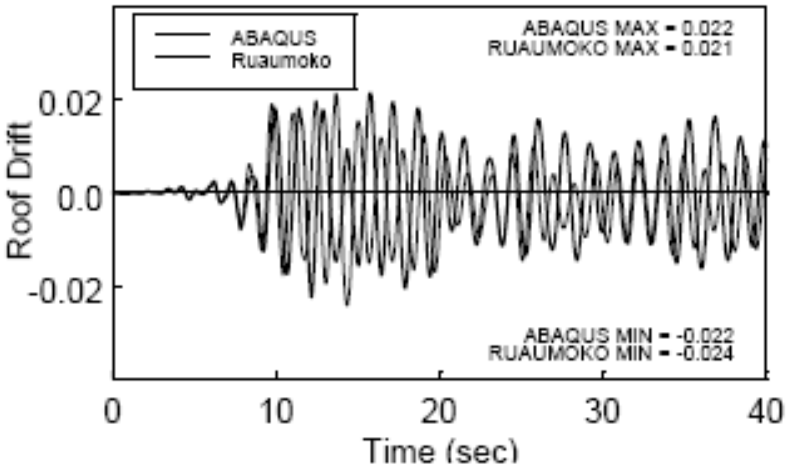

Figure D-8 Roof drift for 1x loading (Richards and Prinz, 2007)

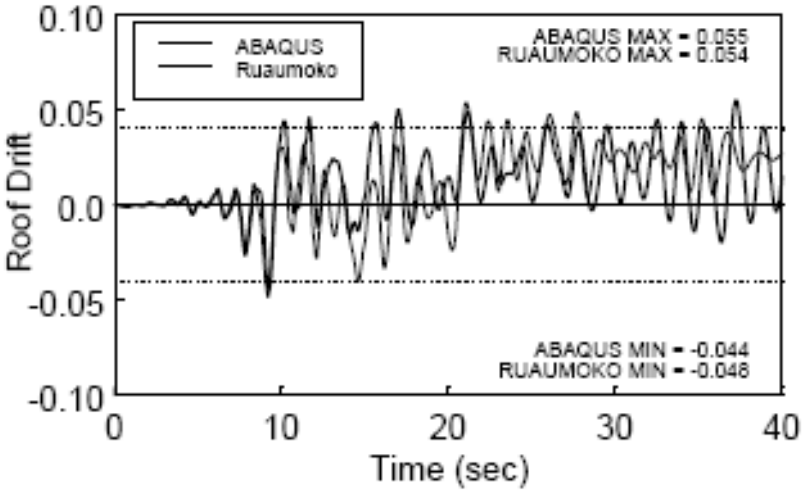

Figure D-9 Roof drift for 3x loading (Richards and Prinz, 2007)

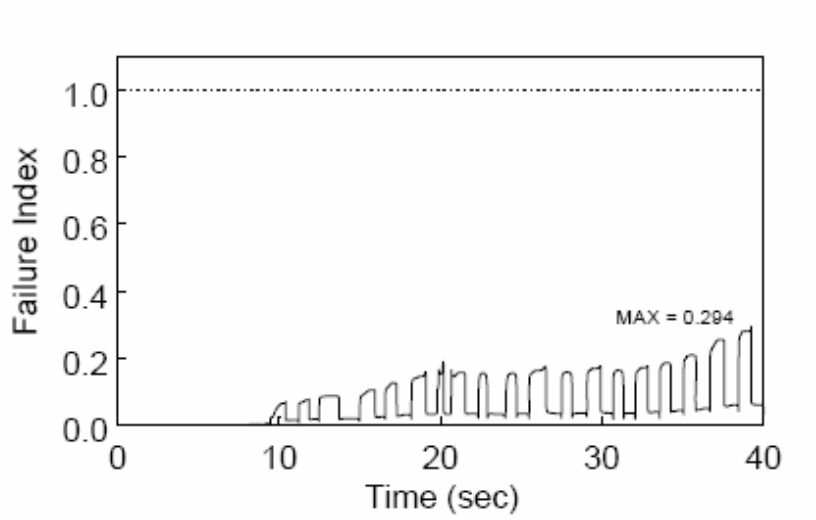

Figure D-10 Failure index at RBS (Richards and Prinz, 2007)

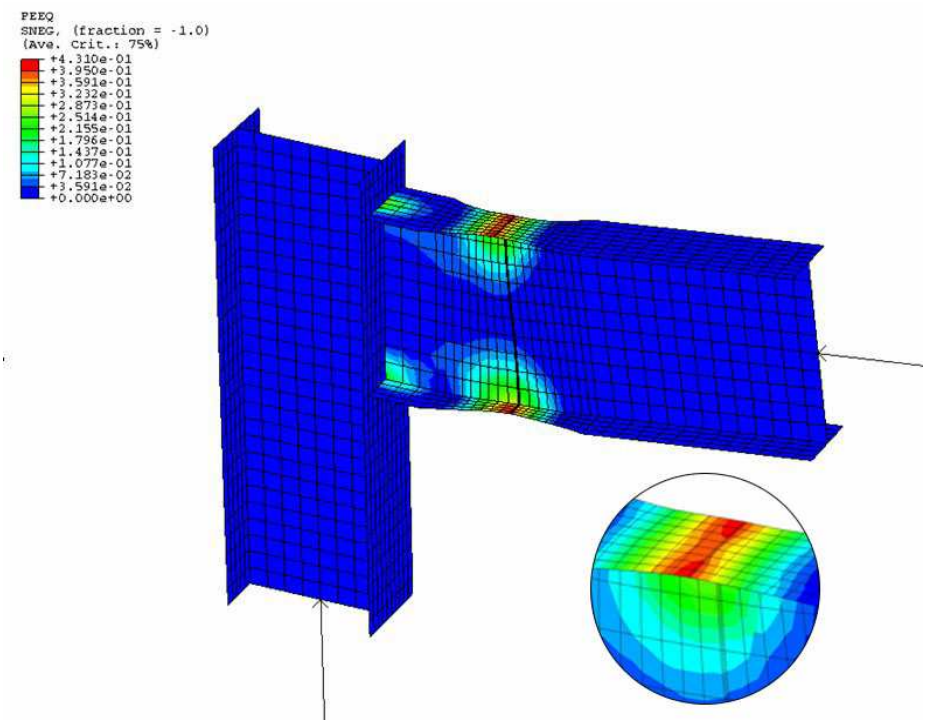

Figure D-11 Plastic strain at RBS

Appendix E. FRAME DESIGN

The tables in this appendix indicate member sizes for thirty-six frames that were designed by Matt Merrell and analyzed by Paul Richards for a study investigating column demands.

Table E-1: 3-Story EBF Designs

	Shape (U.S. designation)			
Member	C_s=0.15	C_s=0.20	C_s=0.25	C_s=0.30
BM1[a, b]	W14×38	W18×40	W21×44	W21×57
BM2	W12×35	W16×36	W16×50	W21×48
BM3	W8×35	W10×30	W14×34	W16×36
BR1[c]	HSS10×10×1/2	HSS12×12×1/2	HSS14×14×1/2	HSS14×14×5/8
BR2	HSS10×10×1/2	HSS10×10×5/8	HSS10×10×5/8	HSS14×14×5/8
BR3	HSS7×7×5/8	HSS10×10×5/8	HSS10×10×5/8	HSS10×10×5/8
C1-C3[d]	W10×45	W10×45	W10×45	W10×68

a. BM1 is beam above first story, BM2 is beam above second story..
b. All beam links are 3 ft long unless otherwise noted
c. BR1 is first story brace, BR2 second story…
d. C1 is first story column, C2 second story…

Table E-2: 9-Story EBF Designs

	Shape (U.S. designation)[a]			
Member	C_s=0.03	C_s=0.05	C_s=0.07	C_s=0.09
BM1[b]	W18×55[c]	W21×83	W21×147	W33×118
BM2	W14×68[c]	W18×65	W24×76	W27×94
BM3	W14×53[c]	W18×76	W12×152	W27×84
BM4	W14×53[c]	W18×60	W12×152	W21×93
BM5	W12×50[c]	W10×100	W18×71	W24×84
BM6	W10×60[c]	W10×88	W18×65	W24×68
BM7	W10×49[c]	W14×53	W10×100	W18×65
BM8	W8×35[c]	W12×40	W14×48	W14×74
BM9	W8×10[d]	W8×31[c]	W8×40	W10×45
BR1	W12×96	W14×132	W12×190	W12×210
BR2	W10×88	W12×87	W12×120	W12×152
BR3-BR4	W10×88	W10×100	W12×120	W12×152
BR5-BR6	HSS10×10×5/8	W10×88	W12×120	W12×136
BR7-BR8	HSS9×9×5/8	W10×68	W12×87	W12×136
BR9	HSS6×6×5/8	W12×45	W12×53	W12×58
C1-C2	W12×152		W12×305	W12×336
C3-C4	W12×96		W12×170	W12×210
C5-C6	W12×96		W12×106	W12×120
C7-C9	W12×96		W12×96	W12×96

a. See notes from Table 7
b. All beam links are 4 ft long unless otherwise noted
c. 3 ft long link
d. 1.5 ft long link

Table E-3: 18-story EBF Designs

	Shape (U.S.)			
Member[a]	C_s=0.03	C_s=0.05	C_s=0.07	C_s=0.09
BM1[b]	W18×46[c]	W21×83	W27×114	W33×118
BM2-BM5	W14×38[c]	W18×60	W24×76	W27×94
BM6	W14×38[c]	W10×112	W21×101	W24×103
BM7	W14×38[c]	W10×112	W12×152	W27×84
BM8	W14×38[c]	W18×55	W21×73	W27×84
BM9	W14×34[c]	W10×100	W21×68	W21×93
BM10	W8×58[c]	W10×100	W16×100	W24×84
BM11	W8×58[c]	W16×67	W21×62	W21×83
BM12	W12×40[c]	W10×88	W18×65	W24×68
BM13	W12×30[c]	W14×61	W10×112	W21×68
BM14	W8×40[c]	W14×48	W10×100	W18×65
BM15	W8×35[c]	W10×54	W14×68	W18×55
BM16	W8×24[c]	W8×48	W12×50	W14×68
BM17	W8×10[d]	W8×31[e]	W10×39	W12×45
BM18	W8×10[d]	W8×18[f]	W8×18[f]	W8×35[c]
BR1	HSS10×10×5/8	W12×96	W12×120	W12×170
BR2-BR6	HSS8×8×5/8	W12×79	W12×96	W12×136
BR7-BR10	HSS8×8×5/8	W12×72	W12×87	W12×120
BR11-BR14	HSS7×7×5/8	HSS10×10×5/8	W12×65	W12×87
BR15-BR16	HSS6×6×5/8	HSS8×8×5/8	W12×65	W12×72
BR17-BR18	HSS6×6×5/8	HSS7×7×1/2	W12×50	W12×53
C1-C2	W12×279	W14×370	W14×550	W14×665
C3-C4	W12×210	W14×311	W14×426	W14×550
C5-C6	W12×170	W14×257	W14×342	W14×426
C7-C8	W12×136	W14×193	W14×283	W14×342
C9-C10	W12×96	W14×145	W14×211	W14×257
C11-C12	W12×96	W14×132	W14×145	W14×176
C13-C14	W12×96	W14×132	W14×132	W14×132
C15-C16	W12×96	W14×132	W14×132	W14×132
C17-C18	W12×96	W14×132	W14×132	W14×132

a. See notes from Table 7
b. All beam links are 4 ft long unless otherwise noted
c. 3 ft long link
d. 1.5 ft long link
e. 3.5 ft long link
f. 2.5 ft long link

Table E-4: 3-Story SCBF and BRBF Designs

	Shape (U.S. designation) or BRBF Brace Area (cm²)							
Member[a]	SCBF C_s=0.15	SCBF C_s=0.20	SCBF C_s=0.25	SCBF C_s=0.30	BRBF C_s=0.15	BRBF C_s=0.20	BRBF C_s=0.25	BRBF C_s=0.30
BR1[b]	HSS7×7×1/2	HSS7×7×1/2	HSS8×8×1/2	HSS8×8×1/2	29	39	52	58
BR2	HSS7×7×1/2	HSS7×7×1/2	HSS7×7×1/2	HSS8×8×1/2	26	32	39	52
BR3	HSS7×7×1/2	HSS7×7×1/2	HSS7×7×1/2	HSS7×7×1/2	16	19	26	29
C1-C3[c]	W12×72	W12×96	W12×136	W12×170	W10×39	W10×49	W10×54	W10×68

a. Brace and column sizes are indicated in the table; beam sizes governed by gravity with all beams W16×40
b. BR1 is first story brace, BR2 second story…
c. C1 is first story column, C2 second story…

Table E-5: 9-Story SCBF and BRBF Designs

	Shape (U.S. designation) or BRBF Brace Area (cm^2)[a]							
Member	SCBF C_s=0.06	SCBF C_s=0.09	SCBF C_s=0.12	SCBF C_s=0.15	BRBF C_s=0.06	BRBF C_s=0.09	BRBF C_s=0.12	BRBF C_s=0.15
BR1	HSS8×8×1/2	HSS9×9×5/8	HSS10×10×5/8	W12×96	42	65	84	100
BR2	HSS8×8×1/2	HSS8×8×1/2	HSS8×8×5/8	HSS9×9×5/8	35	52	65	84
BR3	HSS7×7×1/2	HSS8×8×1/2	HSS8×8×5/8	HSS9×9×5/8	35	52	65	84
BR4	HSS7×7×1/2	HSS8×8×1/2	HSS8×8×5/8	HSS9×9×5/8	32	45	65	77
BR5	HSS7×7×1/2	HSS8×8×1/2	HSS8×8×1/2	HSS9×9×5/8	29	42	58	71
BR6	HSS7×7×1/2	HSS7×7×1/2	HSS8×8×1/2	HSS8×8×5/8	26	35	52	65
BR7	HSS7×7×1/2	HSS7×7×1/2	HSS7×7×1/2	HSS8×8×1/2	19	29	42	52
BR8	HSS7×7×1/2	HSS7×7×1/2	HSS7×7×1/2	HSS8×8×1/2	16	23	29	35
BR9	HSS7×7×1/2	HSS7×7×1/2	HSS7×7×1/2	HSS8×8×1/2	9.7	13	16	19
C1-C2	W14×283	W14×398	W14×500	W14×665	W14×159	W14×233	W14×311	W14×370
C3-C4	W14×176	W14×257	W14×342	W14×426	W14×90	W14×132	W14×176	W14×233
C5-C6	W14×99	W14×145	W14×193	W14×233	W14×61	W14×90	W14×99	W14×120
C7-C9	W14×68	W14×99	W14×120	W14×145	W14×48	W14×48	W14×48	W14×61

a. See all notes from Table E-4

Table E-6: 18-Story SCBF and BRBF Designs

	Shape (U.S. designation) or BRBF Brace Area (cm^2)[a]							
Member	SCBF C_s=0.03	SCBF C_s=0.05	SCBF C_s=0.07	SCBF C_s=0.09	BRBF C_s=0.03	BRBF C_s=0.05	BRBF C_s=0.07	BRBF C_s=0.09
BR1	HSS7x7x1/2	HSS8x8x1/2	HSS10x10x5/8	HSS10x10x5/8	32	52	77	97
BR2-BR3	b	HSS7x7x1/2	HSS8x8x1/2	HSS8x8x5/8	26	42	58	77
BR4-BR5	b	HSS7x7x1/2	HSS8x8x1/2	HSS8x8x5/8	26	42	58	71
BR6-BR7	b	HSS7x7x1/2	HSS8x8x1/2	HSS8x8x5/8	23	39	58	71
BR8-BR9	b	HSS7x7x1/2	HSS8x8x1/2	HSS8x8x5/8	23	35	52	65
BR10-BR11	b	HSS6x6x1/2	HSS7x7x1/2	HSS8x8x1/2	19	32	45	58
BR12-BR13	c	HSS6x6x1/2	HSS7x7x1/2	HSS8x8x1/2	16	26	39	52
BR14	c	HSS6x6x3/8	HSS6x6x1/2	HSS7x7x1/2	13	23	32	39
BR15	c	c	HSS6x6x1/2	HSS6x6x1/2	13	19	26	35
BR16	c	c	HSS6x6x1/2	HSS6x6x1/2	9.7	16	19	26
BR17	c	c	c	c	6.5	9.7	16	19
BR18	c	c	c	c	6.5	6.5	9.7	9.7
C1-C2	W14x283	W14x455	W14x605	W14x730	W14x283	W14x500	W14x665	W14x730
C3-C4	W14x233	W14x398	W14x550	W14x665	W14x233	W14x370	W14x500	W14x665
C5-C6	W14x176	W14x283	W14x398	W14x500	W14x176	W14x311	W14x426	W14x550
C7-C8	W14x132	W14x233	W14x311	W14x426	W14x145	W14x233	W14x311	W14x398
C9-C10	W14x99	W14x159	W14x233	W14x283	W14x99	W14x176	W14x233	W14x283
C11-C12	W14x82	W14x109	W14x132	W14x193	W14x82	W14x120	W14x159	W14x193
C13-C14	W14x53	W14x74	W14x82	W14x109	W14x53	W14x74	W14x90	W14x120
C15-C16	W14x48	W14x48	W14x48	W14x61	W14x48	W14x48	W14x53	W14x61
C17-C18	W14x48	W14x48	W14x48	W14x48	W14x48	W14x48	W14x48	W14x48

a. See all notes from Table E-4
b. HSS 5 1/2x5 1/2x3/8
c. HSS 5 1/2x5 1/2x5/16

REFERENCES

ASCE (2005). "Minimum Design Loads for Buildings and Other Structures." ASCE/SEI 7-05, American Society of Civil Engineers, Reston, VA.

Chi, W.-M., Kanvinde, A. M., and Deierlein, G. G. (2006). "Prediction of ductile fracture in steel connections using SMCS criterion." *J.l of Struct. Eng.*, 132(2), 171-181.

Coy, B. B. (2007). "Buckling-restrained brace connection design and testing." masters thesis, Brigham Young University, Provo, UT.

Fell, B. V., Myers, A. T., Deierlein, G. G., and Kanvinde, A. M. (2006). "Testing and simulation of ultra-low cycle fatigue and fracture in steel braces." Proceedings of the 8th U.S. National Conference on Earthquake Engineering, San Francisco, CA, Paper No. 587.

Gupta, A., Krawinkler, H. (1999). "Prediction of seismic demands for SMRFs with ductile connections and elements." *Report No. SAC/BD-99/06,* SAC Joint Venture, Sacramento, CA.

Hancock, J. W., and Mackenzie, A. C. (1976). "On the mechanics of ductile failure in high-strength steel subjected to multi-axial stress-states." *J. Mech. Phys. Solids.*, 24(3), 147-160.

HKS (2006). *ABAQUS Standard Users Manu, Version 6.4l*, Hibbitt, Karlsson, and Sorensen, Inc., Providence, RI.

Kanvinde, A. M and Deierlein, G. G., 2007. "Cyclic void growth model to assess ductile fracture initiation in structural steels due to ultra low cycle fatigue." *J.l of Eng. Mechanics*, 133(6), 701-712.

Richards, P. W., and Prinz, G. S. (2007). "Nonlinear time-history analysis of refined mesh steel structures." Proceedings of the 9th Canadian Conference on Earthquake Engineering, Ontario, Canada, Paper No. 1365.

Richards, P.W., Ruiz-Garcia, J., and Uang, C-M., 2002. “Cyclic testing of deep-column RBS steel moment connections for Providence Saint Joseph Medical Center.” *Report No. TR-2002/05*,Department of Structural Engineering, University of California at San Diego, La Jolla, CA.

SAC Joint Venture., 2000. “Recommended seismic design criteria for new steel moment-frame buildings,” prepared by the SAC Joint Venture for the Federal Emergency Management Agency, *Rep No.FEMA-350*, FEMA, Washington D.C.